CNT-polymer nanocomposites under frictional contact conditions

Luis Rodríguez-Tembleque[a,∗], Enrique García-Macías[a], Andrés Sáez[a]

[a]Escuela Técnica Superior de Ingeniería, Universidad de Sevilla, Camino de los Descubrimientos s/n , Sevilla E-41092, Spain.

Highlights

- Indentation response of aligned and randomly distributed CNT-polymer nanocomposites.

- A contact friction law has been considered to analyze the effect of fillers orientation.

- Micromechanics is based on the concept of equivalent solid fiber: a portion of matrix material and an embedded CNT.

- Coupled effect of filler waviness and agglomeration is investigated.

Abstract

The unique intrinsic physical properties of Carbon NanoTubes (CNTs) suggest that they are ideal fillers for high-performance composites. Although some experimental studies have revealed the potential of these nanoparticles to tailor the tribological properties of polymer-based composites, the number of theoretical studies on the characterization of their frictional behavior is still very low. This paper is aimed at filling this lacuna by addressing the theoretical analysis of the indentation response of CNT-polymer nanocomposites. To do so, it is first necessary to compute the overall mechanical properties of CNT-polymer composites. Secondly, these properties must be used to evaluate the macroscopic indentation response of the composites. In this work, an extended Mori-Tanaka approach is used to extract the constitutive properties of CNT-polymer nanocomposites. On the basis of ad hoc Eshelby's tensors accounting for particular wavy filler geometries, along with a two-parameter agglomeration model, the homogenization process is performed considering the coupled effect of fillers' waviness and agglomeration. Afterward, a 3D boundary element formulation for contact modeling is applied to study the indentation response of these nanocomposites. The main objective of this paper focuses on analysing the influence of micromechanical features such as fiber content, orientation, waviness, and dispersion on the indentation response of CNT-polymer nanocomposites. Detailed parametric analyses are presented to characterize this phenomenon under frictional contact conditions. The numerical results demonstrate that fillers' waviness and agglomeration have a coupled detrimental effect on the macroscopic response of CNT-reinforced composites.

Keywords: Carbon nanotube, Indentation, Friction, Agglomeration, Micromechanics, Waviness

1. Introduction

In recent years, a broad cross-section of the scientific community has been attracted by Carbon NanoTubes (CNTs) due to their unique intrinsic physical properties. Their remarkable mechanical, thermal and electrical properties open a vast range of applications as reinforcing fillers for high strength composites [1], as well as smart materials with self-sensing capabilities [2–4]. In particular, there exists an increasing interest for the development of polymer-based nanocomposites. Thanks to their excellent corrosion resistance, relatively low unit cost, facile processing and recyclability, polymers are widely used in an extensive and diverse range of tribological areas [5]. The indentation response under frictional contact is a crucial feature for most vital engineering components and systems in industrial applications such as gears, bearings, artificial human joint bearing surfaces, high performance coatings, tires, etc. [6]. The specific development of CNT-polymer nanocomposites allows to obtain new materials with superior indentation resistance and tribological behavior [7, 8]. Although some studies have evidenced the promising potential of CNTs to tailor the tribological properties of polymer-based composites, the number of theoretical studies concerning the frictional behavior of carbon nanotube reinforced composites is still very scant.

∗corresponding author
Email address: `luisroteso@us.es` (Luis Rodríguez-Tembleque)

In this sense, previous studies have shown that Carbon Nanotube-Reinforced Composite (CNTRC) materials exhibit more stable frictional coefficients and lower wear rates [9–12]. Indentation techniques on thin-films and bulk forms have been studied not only to have a better understanding of these materials under contact conditions but also to measure their mechanical properties in CNTRCs [13, 14] and in composites doped with Vertically Aligned Carbon Nanotubes (VACNT) [15–20] or with horizontal aligned CNTs [21]. As observed in the tribological response, the indentation response of CNTRCs is highly affected by micromechanical aspects such as alignment and agglomeration. Computational virtual indentation tests allows to characterize the mechanical properties of CNTRCs. In addition, this type of techniques has a great potential to design and maximize the effectiveness of the reinforcement and therefore the properties of the CNTRC. Some works based on the Finite Element Method (FEM) [22–24] have modeled the indentation response of CNTRC. Le and Huang [22] consider explicitly the CNTs and Liu et al. [23, 24] assume the effective mechanical properties of nanoreinforced composites. However, as observed in those works, a very fine mesh must be considered to approximate CNTs inclusions and the contact problem between the indenter and the specimen. The Boundary Element Method (BEM) [25, 26] is recognized as an accurate and efficient numerical tool for studying contact and interface problems. A few works have dealt with the problem of CNTRC modeling using BEM [27–29], taking into account the microstructural approximation of the CNT-polymer system. Although, in all these BEM formulations, no contact indentation conditions were considered.

Recent works on the tribological properties of CNT reinforced polymer composites showed that it would be desirable to control the alignment and the dispersion of the nanoinclusions in the matrix [30, 31]. In this context, aligned and well-dispersed CNTs are desirable to develop new advanced composites for more demanding applications and high-performance tribomaterials [21, 32, 33]. However, due to the electronic configuration of the tube walls of CNTs, as well as their high specific surface area, CNTs tend to agglomerate in bundles resulting in non-homogeneous filler dispersions. In addition, due to their low bending stiffness, CNTs within polymer matrices usually present a certain degree of waviness. Notwithstanding there exists a number of aligning techniques such as the application of magnetic fields [34] and electrospinning [35], as well as dispersing methodologies such as the use of dispersants or sonication, obtaining uniform dispersions of aligned CNTs remains an enormously challenging task. Furthermore, the cost and complexity of these manufacturing processes limit the scalability for this type of configurations [36]. For this reason, the analysis of accurate filler microstructures, including waviness and agglomeration effects, is of pivotal importance for assisting the design of these composites. Despite considerable efforts can be found in the literature on this respect, most studies limit themselves to the study of waviness and agglomeration acting independently.

In light of the previous literature review, this work is aimed at investigating the indentation response of CNTRC under frictional contact conditions with CNT waviness and agglomeration effects. The effective constitutive properties of CNTRCs are predicted by an extended Mori-Tanaka homogenization approach. The agglomeration of CNTs in bundles is analyzed by means of a two-parameter agglomeration model. In addition, an ad hoc Eshelby's approach for accounting for particular wavy filler microstructures. In virtue of the ad hoc definition of the Eshelby's tensor of wavy fillers, it is possible to study the coupled effect of waviness and agglomeration. The analysis of the indentation response of CNTRCs is conducted by a 3D BEM formulation. A contact constitutive friction law for ACNT fibers is considered and incorporated to an augmented Lagrangian contact resolution scheme, which allows us to solve the contact problem taking into account both the mechanical and the tribological anisotropic characteristics (i.e. anisotropic bulk properties and anisotropic wear and frictional conditions). The proposed methodology is applied to study the indentation response of a CNTRC half-space configurations, and how micro and nanomechanics affect the contact compliances. The potential of the present work is illustrated by detailed parametric analyses on the influence of microstructural features such as filler orientations, filler content, as well as the sliding direction and the thickness of the film on the normal and tangential contact forces. Finally, the coupled effect of waviness and agglomeration on the indentation response is investigated. The results demonstrate that both mechanisms have detrimental influence on the overall stiffness and, when act simultaneously, their effect add up. Overall, the present work presents a comprehensive micromechanics-based 3D formulation for the analysis of the tribological response of CNTRCs, including a realistic definition of the microstructural features.

The remainder of this work is organized as follows: Section 2 presents the problem description, Section 3 presents the micromechanical constitutive models for CNTRCs. Section 4 overviews the basic governing equations of the indentation response and the non-linear contact conditions. The literature on BEM formulations is quite extensive, so in Section 5 we briefly present the basic ideas of a boundary element formulation to solve contact problems. Section 6 presents the numerical results and discussion and, finally, Section 7 concludes the paper.

2. Problem description

Let us consider an elastic half-space Ω^1 and an elastic indentor Ω^2 over in $\mathbb{R}^3$, see Fig. 1. The boundary of Ω^l ($l = 1, 2$), $\partial\Omega^l$, is divided into three disjoint parts: $\partial\Omega^l_t$ with prescribed tractions $\tilde{t}^l_i$ ($i = 1, 2, 3$), $\partial\Omega^l_u$ with imposed displacements $\tilde{u}^l_i$ and $\partial\Omega^l_c$ represents the potential contact surfaces, which have outward unit normal vectors n^l_i. Under small displacement and strain assumption, these boundaries are almost coincident (i.e. $\partial\Omega^1_c \simeq \partial\Omega^2_c$) so we can define a common contact surface $\partial\Omega_c$ with a normal vector $n_{c,i} \simeq n^1_i \simeq -n^2_i$. Moreover, the infinitesimal strain tensor ε_{ij} can be obtained from derivatives of the displacements field u_i in $\Omega^1 \cup \Omega^2$ as: $\varepsilon_{ij} = (u_{i,j} + u_{j,i})/2$ in $\Omega^1 \cup \Omega^2$.
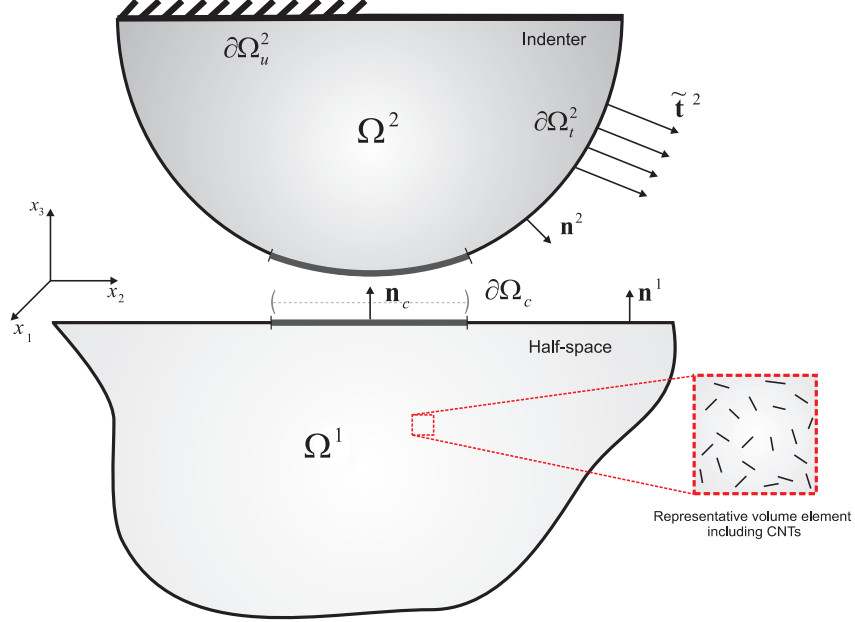

Figure 1: The physical setting. Domain Ω^1 is the CNT reinforced composite domain and Ω^2 is the indenter.

On the domains Ω^l, assuming static loading conditions, the mechanical equilibrium equations in the absence of body forces are:

$$\begin{aligned}
\sigma_{ij,j} &= 0 && \text{in} \quad \Omega^1 \cup \Omega^2, \\
\sigma_{ij} n^l_j &= \tilde{t}_i && \text{on} \quad \partial\Omega^1_t \cup \partial\Omega^2_t, \\
\sigma^1_{ij} n_{c,j} &= -\sigma^2_{ij} n_{c,j} = p_i && \text{on} \quad \partial\Omega_c,
\end{aligned} \quad (1)$$

with σ_{ij} being the components of Cauchy stress tensor, n_i the unit normal on $\partial\Omega^1_t \cup \partial\Omega^2_t$, p_i is the contact traction and σ^1_{ij} and σ^2_{ij} are restrictions of σ_{ij} to a particular domain Ω^l_t. In this work, summation convention is adopted unless explicitly stated otherwise (so repeated indexes imply sum). Finally, the stress and strain tensors for a general anisotropic linear elastic material are related through the linear constitutive law as follows:

$$\sigma_{ij} = C_{ijkl}\varepsilon_{kl}, \quad (2)$$

where C_{ijkl} denotes the elastic stiffness tensor, which is positive definite and satisfies the following symmetries: $C_{ijkl} = C_{jikl} = C_{ijlk} = C_{klij}$.

3. Micromechanics constitutive modeling of CNTRCs

In this work, the macroscopic elastic moduli of CNT-reinfoced polymer composites are computed by mean-field homogenization approaches. In particular, three different filler arrangements are considered, namely composites doped with uniformly distributed straight CNTs in Subsection 3.1, composites doped with uniformly distributed wavy CNTs in Subsection 3.2, and composites doped with heterogeneous dispersions of CNTs in Subsection 3.3. Throughout this section, a boldface letter stands for fourth-order tensor, and a colon between two tensors denotes inner product, $\mathbf{A} : \mathbf{B} \equiv A_{ijkl}B_{klmn}$.

3.1. Composites doped with uniformly distributed straight CNTs.

Let us define the Representative Volume Element (RVE) sketched in Fig. 2 of a polymer matrix doped with a sufficient number of straight CNTs in such a way that, from a statistical perspective, the RVE represents the composite as a whole [37]. The matrix is defined as isotropic with Young's modulus E_m and Poisson's ratio v_m, and perfect bonding between phases is assumed. In order to define the orientation of the inclusions, a local coordinate system $\{1', 2', 3'\}$ is fixed at each filler as represented in Fig. 2. The constitutive matrix for inclusions with transversely isotropic properties (1' is the axis of material symmetry) in the local coordinate system takes the form:
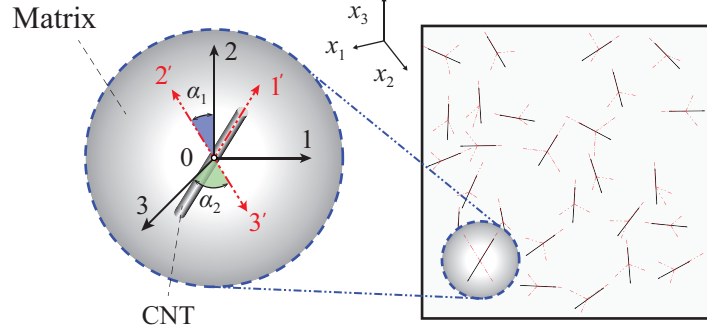

Figure 2: RVE of polymer matrix doped with straight CNTs.

$$\mathbf{C}_r = \begin{bmatrix} n_r & l_r & k_r - m_r & 0 & 0 & 0 \\ l_r & k_r + m_r & l_r & 0 & 0 & 0 \\ k_r - m_r & l_r & k_r + m_r & 0 & 0 & 0 \\ 0 & 0 & 0 & m_r & 0 & 0 \\ 0 & 0 & 0 & 0 & p_r & 0 \\ 0 & 0 & 0 & 0 & 0 & p_r \end{bmatrix} \tag{3}$$

where k_r, l_r, m_r, n_r and p_r are fiber Hill's elastic moduli; k_r is the plane-strain bulk modulus normal to the fiber direction, n_r is the uniaxial tension modulus in the fiber direction, l_r is the associated cross modulus, m_r and p_r are the shear moduli in planes normal and parallel to the fiber direction, respectively. The material properties of the composite can be expressed in terms of engineering constants as [38, 39]:

$$n_r = \frac{E_{11}(1 - v_{23})}{1 - v_{23} - 2v_{21}v_{12}} \tag{4}$$

$$l_r = \frac{v_{12}E_{22}}{1 - v_{23} - 2v_{21}v_{12}} \tag{5}$$

$$m_r = G_{23} \tag{6}$$

$$p_r = G_{12} \tag{7}$$

$$k_r = \frac{E_{22}}{2(1 - v_{23} - 2v_{21}v_{12})} \tag{8}$$

Considering the transverse isotropy of the fillers, the shear modulus in the plane of isotropy G_{23} can be evaluated as:

$$G_{23} = \frac{E_{22}}{2(1 + v_{23})} \tag{9}$$

In this context, a widely used approach to compute the macroscopic elastic moduli of the RVE is the micromechanics model of Eshelby-Mori-Tanaka [40]. The Mori-Tanaka method allows to extend the theory of Eshelby [41, 42], restricted to one single inclusion within a semi-infinite elastic, homogeneous and isotropic medium, to the case of multiple inhomogeneities embedded in a finite domain. According to Benveniste's revision [43], the effective stiffness tensor provided by the Eshelby-Mori-Tanaka model can be written as:

$$\mathbf{C} = \mathbf{C}_m + f_r \langle (\mathbf{C}_r - \mathbf{C}_m) : \mathbf{A} \rangle : (f_m \mathbf{I} + f_r \langle \mathbf{A} \rangle)^{-1} \tag{10}$$

4

where f_r and f_m denote the filler and matrix volume fractions, respectively, $\mathbf{I}$ the fourth-order identity tensor, and $\mathbf{C}_m$ the stiffness tensor of the matrix. The tensor $\mathbf{A}$ stands for the dilute mechanical strain concentration tensor defined as:

$$\mathbf{A} = \left[\mathbf{I} + \mathbf{S} : (\mathbf{C}_m)^{-1} : (\mathbf{C}_r - \mathbf{C}_m)\right]^{-1} \tag{11}$$

with $\mathbf{S}$ being the Eshelby's tensor, whose definition is well documented in reference [44]. The terms enclosed with angle brackets in Eq. (10) represent the average value of the corresponding term over all orientations. In order to conduct these orientational averages, the orientation of a filler aligned in the local axis 1' is defined with respect to the material coordinate system by two Euler angles, α_1 and α_2, as indicated in Fig. 2. The base vectors $\mathbf{e}$ and $\mathbf{e}'$ of the global $\{1, 2, 3\}$ and local $\{1', 2', 3'\}$ coordinate systems are related via the transformation matrix $\mathbf{g}$ as $e'_i = g_{ij}e_j$. Thus, the coordinate transformation of a fourth-order tensor $\mathbf{P}$ into the local coordinate system is explicitly represented in terms of the transformation matrix as $P'_{ijkl} = g_{ip}g_{jq}g_{kr}g_{ls}P_{pqrs}$. Due to the high number of inclusions contained in the RVE, the description of their orientation field is of statistical nature. The probability of finding a filler in an infinitesimal range of angles $[\alpha_1, \alpha_1 + d\alpha_1] \times [\alpha_2, \alpha_2 + d\alpha_2]$ is given by $\Omega(\alpha_1, \alpha_2) \sin \alpha_1 d\alpha_1 d\alpha_2$, with $\Omega(\alpha_1, \alpha_2)$ being the so-called Orientation Distribution Function (ODF). Let us note that, in the case of randomly oriented fillers, the ODF is defined as a constant of value $\Omega = 1/2\pi$. Hence, the orientational average of any tensorial function $\mathbf{F}(\alpha_1, \alpha_2)$ is defined through:

$$\langle \mathbf{F} \rangle = \int_0^{2\pi} \int_0^{\pi/2} \mathbf{F}(\alpha_1, \alpha_2)\Omega(\alpha_1, \alpha_2) \sin \alpha_1 d\alpha_1 d\alpha_2 \tag{12}$$

Some inconsistencies in the Eshelby-Mori-Tanaka method have been reported in the literature, including diagonally asymmetric stiffness tensors for arbitrary filler orientation distributions, as well as violation of the Hashin-Shtrikman-Walpole bounds for randomly oriented filler configurations [43]. As an alternative, Schjødt-Thomsen and Pyrz [45] proposed an extended Eshelby-Mori-Tanaka method that averts the inconsistencies mentioned above. This approach utilizes a direct orientational average of the Eshelby-Mori-Tanaka stiffness tensor for the case of perfectly aligned fillers as:

$$\mathbf{C} = \left\langle \mathbf{C}_m + f_r (\mathbf{C}_r - \mathbf{C}_m) : \mathbf{A} : (f_m\mathbf{I} + f_r\mathbf{A})^{-1} \right\rangle \tag{13}$$

3.2. Composites doped with uniformly distributed wavy CNTs.

It has been extensively reported in the literature that due to their high aspect ratio, as well as a very low bending stiffness, carbon nanotubes usually exhibit a certain degree of waviness [46–48]. In the present work, the simulation of the wavy state of CNTs is performed by means of the helical approach proposed by Shi *et al*. [49]. Fig. 3 schematically represents the parametrization of a helical CNT. This three-dimensional curve is fully defined by its diameter D, spiral angle θ, and polar angle φ. The length L of the curved CNT is related to these parameters by:

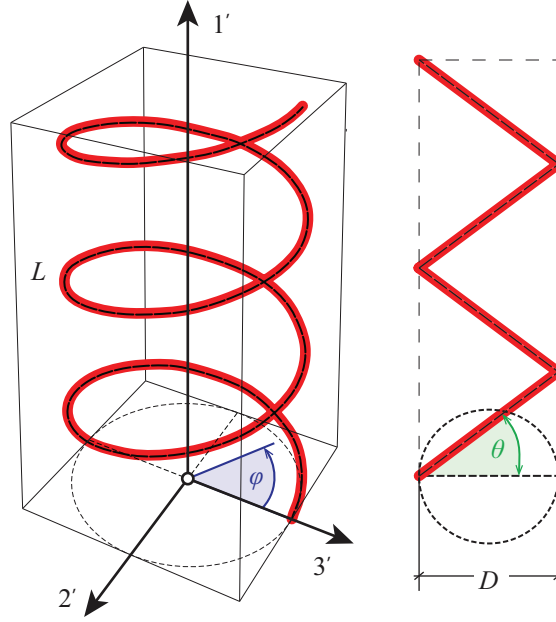$$L = \frac{\varphi D}{2 \cos \theta} \tag{14}$$

Figure 3: Helical model of a curved CNT.

The CNT waviness is governed by the spiral angle, θ. For example, $\theta = \pi/2$ corresponds to a straight CNT, while $\theta = 0$ represents a circular CNT. In this context, the direct application of the MT fails to accurately reproduce the microstructure of composites doped with wavy fillers. As discussed in reference [49], the MT estimates for random filler arrangements are insensitive to waviness. For this reason, the ad hoc Eshelby's tensor proposed by Yanase *et al.* [50] is adopted in this work to account for waviness effects. According to this model, the effective stiffness of wavy CNT-reinforced composites at a dilute regime is evaluated by the following integral:

$$\overline{\mathbf{C}} = \frac{1}{\delta} \int_0^\delta \mathbf{C}^*(\theta, s)\mathrm{d}s \tag{15}$$

with $\mathbf{C}^*$ being the solution of the Eshelby's equivalent problem as:

$$\mathbf{C}^* = \mathbf{C}_m + f_r\left(\mathbf{C}_f - \mathbf{C}_m\right) : \mathbf{A} \tag{16}$$

In order to reproduce Eq. (15) with the Eshelby's equivalent inclusion method, an ad hoc Eshelby's tensor, $\overline{\mathbf{S}}$, was proposed by Yanase and co-authors as follows:

$$\overline{\mathbf{S}} = \lim_{f_r \to 0}\left[f_r\left((\mathbf{C}_m)^{-1} : \overline{\mathbf{C}} - \mathbf{I}\right)^{-1} - \left(\mathbf{C}_f - \mathbf{C}_m\right)^{-1} : \mathbf{C}_m\right] \tag{17}$$

where the limit is taken to exclude the far-field interaction. Now, the effective stiffness of fully aligned wavy CNT-reinforced composites at non-dilute regimes can be computed by the Eshelby-Mori-Tanaka method as:

$$\mathbf{C} = \mathbf{C}_m + f_r\left(\mathbf{C}_r - \mathbf{C}_m\right) : \mathbf{A}^* : (f_m\mathbf{I} + f_r\mathbf{A}^*)^{-1} \tag{18}$$

where

$$\mathbf{A}^* = \left[\mathbf{I} + \overline{\mathbf{S}} : \mathbf{C}_m^{-1} : \left(\mathbf{C}_f - \mathbf{C}_m\right)\right]^{-1} \tag{19}$$

Here, the extended Eshelby-Mori-Tanaka approach proposed by Schjødt-Thomsen and Pyrz [45] in Eq. (13) can be readily applied to Eq. (18) in order to account for randomly oriented wavy filler arrangements.

3.3. Composites doped with heterogeneous dispersions of CNTs.

Another important phenomenon to be taken into account in the simulation of CNT-based composites is the appearance of non-uniform spatial distributions of nanoinclusions. Although there exists a variety of techniques to improve the dispersion of fillers, including the use of dispersants or sonication, uniform dispersions of CNTs at moderate filler contents is still an intricate task. The tendency of nanotubes to form agglomerates is ascribed to the electronic configuration of the tube walls and their high specific surface, what favors the appearance of large van der Waals (vdW) attraction forces among nanotubes [51–53]. It has been reported in the literature that CNT

agglomerates act as defects in the microstructure, exhibiting considerable weakening effects on the macroscopic mechanical properties [54]. In order to incorporate agglomeration effects in the numerical simulations, the two-parameter agglomeration model introduced by Shi *et al.* [49] is adopted in this work. This approach distinguishes two different regions, one with high filler concentration, corresponding to clusters, and another with low filler concentration, that is to say, the surrounding composite. Hence, the total volume of CNTs, V_r, dispersed in V, can be divided into the following two parts:

$$V_r = V_r^{bundles} + V_r^m \tag{20}$$

where $V_r^{bundles}$ and V_r^m denote the volumes of CNTs dispersed within the bundles and in the surrounding matrix, respectively. In order to characterize the agglomeration degree, two parameters, ξ and ζ, are introduced as follows:

$$\xi = \frac{V_{bundles}}{V}, \quad \zeta = \frac{V_r^{bundles}}{V_r} \tag{21}$$

where $V_{bundles}$ is the volume occupied by the bundles in the RVE. The agglomeration parameter ξ represents the volume ratio of bundles with respect to the total volume of the RVE. On the other hand, ζ stands for the volume ratio of CNTs within the bundles with respect to the total volume of fillers. After some manipulations, the CNT volume fractions in the bundles and the surrounding composite, c_1 and c_2, respectively, can be expressed as:

$$c_1 = f_r \frac{\zeta}{\xi}, \quad c_2 = f_r \frac{1-\zeta}{1-\xi} \tag{22}$$

It is extracted from Eq. (22) that $\zeta \geq \xi$ must be fulfilled in order to impose a higher filler concentration in the bundles. The limit case $\zeta = \xi$ represents an uniform distribution of fillers ($c_1 = c_2$), whilst the heterogeneity degree grows ($c_1 \geq c_2$) for larger values of ζ up to $\zeta = \min(1, \xi/f_r)$. Hence, the homogenization process is conducted through two separate steps as outlined in Fig. 4. Firstly, the overall constitutive tensors of the bundles, $\mathbf{C}^{in}$, and the surrounding composite, $\mathbf{C}^{out}$, are obtained with polymer and CNTs as matrix and reinforcing phases, considering filler volume fractions of c_1 and c_2, respectively. To this aim, the previously overviewed homogenization approach (Eq. (13) or Eq. (18)) can be applied by considering $f_r = c_i$, $i = 1,2$. Secondly, the overall constitutive tensor of the composite, $\mathbf{C}^*$, is computed considering the surrounding composite as matrix and bundles as ellipsoidal inclusions ($f_r = \xi$).
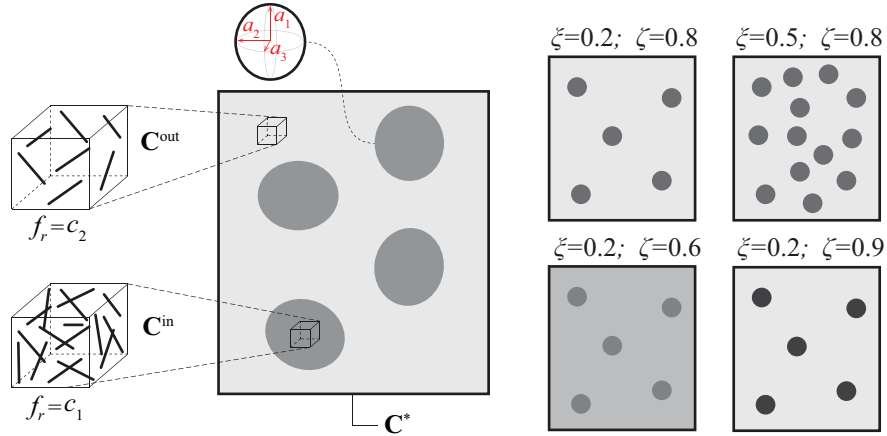

Figure 4: Schematic illustration of the variation of the parameters ξ and ζ of the two-parameter agglomeration model.
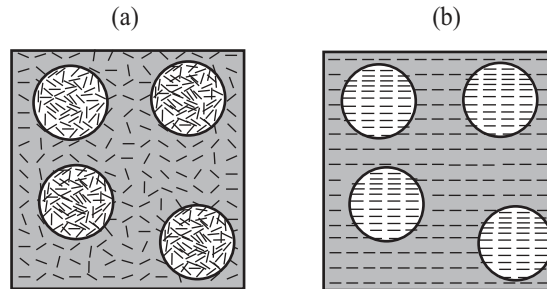

Figure 5: Schematic representation of agglomeration configurations: (a) randomly oriented and (b) uniaxially aligned CNTs.

In this work, two different agglomeration configurations are investigated, including randomly oriented and fully aligned fillers as sketched in Fig. 5. In the case of randomly oriented fillers (Fig. 5 (a)), both the clusters and the surrounding matrix are isotropic and, therefore, the resulting composite exhibits isotropic elastic properties [55–57]. Conversely, in the case of fully aligned filler arrangements (Fig. 5 (b)), both the clusters and the surrounding matrix are transversely isotropic. Therefore, it is necessary to use Eshelby's tensors according to such configurations. Lin and Mura [58] gave expressions for the elastic fields of spheroidal inclusions ($a_2=a_3 \neq a_1$) in a transversely isotropic matrix with symmetry plane 2′-3′. The bundle aspect ratio a_1/a_3 is denoted by ρ. For a transversely isotropic matrix (in the case of Fig. 5 (b), the surrounding matrix), the elastic moduli are denoted by:

$$d = C_{11}^{out}, \quad e = \frac{1}{2}(C_{11}^{out} - C_{12}^{out}), \quad f = C_{44}^{out},$$
$$g = C_{13}^{out} + C_{44}^{out}, \quad h = C_{33}^{out} \tag{23}$$

where C_{ij}^{out} are the components in Voigt notation of the surrounding matrix. The Eshelby's tensor **S** is calculated as [58]:

$$S_{ijmn} = \frac{1}{8\pi} C_{pqmn}^{out} \left(\overline{G}_{ipjq} + \overline{G}_{jpiq} \right) \tag{24}$$

The non-zero components of $\overline{G}_{ijkl}$ are given by:

$$\overline{G}_{1111} = \overline{G}_{2222} = \frac{\pi}{2} \int_0^1 \Delta(1-x^2) \left\{ \left[f(1-x^2) + h\rho^2 x^2 \right] \right.$$
$$\left[(3e+d)(1-x^2) + 4f\rho^2 x^2 \right] - g^2\rho^2 x^2(1-x^2) \right\} dx, \tag{25}$$

$$\overline{G}_{3333} = 4\pi \int_0^1 \Delta\rho^2 x^2 \left[d(1-x^2) + f\rho^2 x^2 \right] \left[e(1-x^2) + f\rho^2 x^2 \right] dx, \tag{26}$$

$$\overline{G}_{1212} = \overline{G}_{2121} = \frac{\pi}{2} \int_0^1 \Delta(1-x^2) \left\{ \left[f(1-x^2) + h\rho^2 x^2 \right] \right.$$
$$\left[(e+3d)(1-x^2) + 4f\rho^2 x^2 \right] - 3g^2\rho^2 x^2(1-x^2) \right\} dx, \tag{27}$$

$$\overline{G}_{1313} = \overline{G}_{2323} = 2\pi \int_0^1 \Delta\rho^2 x^2 \left\{ \left[(d+e)(1-x^2) + 2f\rho^2 x^2 \right] \right.$$
$$\left[f(1-x^2) + h\rho^2 x^2 \right] - g^2\rho^2 x^2(1-x^2) \right\} dx, \tag{28}$$

$$\overline{G}_{3131} = \overline{G}_{3232} = 2\pi \int_0^1 \Delta(1-x^2) \left\{ \left[d(1-x^2) + f\rho^2 x^2 \right] \right.$$
$$\left[e(1-x^2) + f\rho^2 x^2 \right] \right\} dx, \tag{29}$$

$$\overline{G}_{1122} = \frac{\pi}{2} \int_0^1 \Delta(1-x^2)^2 \left\{ g^2\rho^2 x^2 - (d-e) \left[f(1-x^2) \right. \right.$$
$$\left. h\rho^2 x^2 \right] \right\} dx, \tag{30}$$

$$\overline{G}_{1133} = \overline{G}_{2233} = -(2\pi) \int_0^1 \Delta g\rho^2 x^2(1-x^2) \left[e(1-x^2) + f\rho^2 x^2 \right] dx \tag{31}$$

where:

$$\Delta^{-1} = \left[e(1-x^2) + f\rho^2 x^2 \right] \left\{ \left[d(1-x^2) + f\rho^2 x^2 \right] \right.$$
$$\left[f(1-x^2) + h\rho^2 x^2 \right] - g^2\rho^2 x^2(1-x^2) \right\} \tag{32}$$

4. Frictional contact constitutive laws

4.1. Unilateral contact law

The Signorini's unilateral contact conditions in $\partial\Omega_c$ can be defined as:

$$g_n \geq 0, \quad p_n \leq 0, \quad g_n p_n = 0, \tag{33}$$

where $p_n = \mathbf{p} \cdot \mathbf{n}_c$ is the normal contact pressure and $g_n = (g_o + u_n)$ is the contact gap, g_o being the initial gap between the bodies and $u_n = (\mathbf{u}^2 - \mathbf{u}^1) \cdot \mathbf{n}_c$ being the relative displacements. These normal contact constraints, as presented in Eq. (33), can be reformulated in a more compact form as:

$$p_n - \mathbb{P}_{\mathbb{R}_-}(p_n^*) = 0, \tag{34}$$

where $\mathbb{P}_{\mathbb{R}_-}(\bullet)$ is the normal projection function ($\mathbb{P}_{\mathbb{R}_-}(\bullet) = min(0, \bullet)$) and $p_n^* = p_n + r_n g_n$ is the augmented normal traction. The parameter r_n is the normal dimensional penalization parameter ($r_n \in \mathbb{R}^+$).

4.2. Frictional contact law

According to experimental works in the literature [30, 31], Aligned Carbon NanoTubes (ACNT) reinforced composites exhibit a frictional response which is clearly affected by the fiber orientation relative to the sliding direction. Fig. 6 (a) shows an ACNT reinforced composite indicating the longitudinal, transverse and normal sliding directions, and their corresponding friction coefficients. In this case, the friction law can be accurately approximated by an orthotropic friction law when the fiber directions are parallel to the contact surface (see Fig. 6 (b) and Fig. 6 (c)). Different works in the literature [59–63] have studied and developed different anisotropic friction models which define the admissible region for contact tractions and the sliding rules.

The generic form of the orthotropic friction cone can be written as:

$$f(\mathbf{p}_t, p_n) = \|\mathbf{p}_t\|_\mu - |p_n| = 0, \tag{35}$$

where $\mathbf{p}_t = \mathbf{p} - p_n \mathbf{n}_c$, and $\| \bullet \|_\mu$ denotes the elliptic norm $\|\mathbf{p}_t\|_\mu = \sqrt{(p_{e_1}/\mu_1)^2 + (p_{e_2}/\mu_2)^2}$, being μ_1 and μ_2 the principal friction coefficients in the directions $\{e_1, e_2\}$.
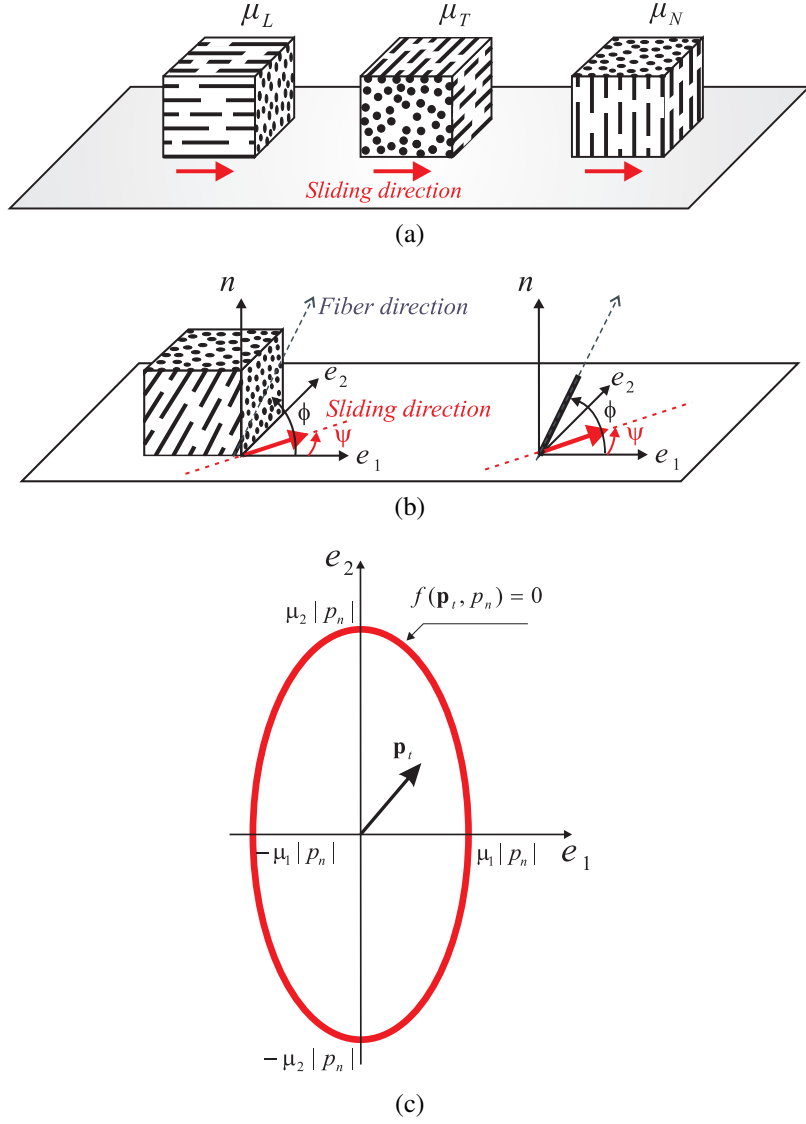
Figure 6: (a) Schematic diagram of ACNT reinforced composite indicating the longitudinal, transverse and normal sliding directions. (b) Arbitrary ACNT direction. (c) Elliptic friction law as a function of the CNT orientation.

The Coulomb friction restriction defines the admissible region for tangential contact tractions ($f(\mathbf{p}_t, p_n) \leq 0$: $\|\mathbf{p}_t\|_\mu \leq |p_n|$) and it can be summarized as:

$$\|\mathbf{p}_t\|_\mu < |p_n| \Rightarrow \quad \dot{\mathbf{g}}_t = \mathbf{0} \quad \text{on} \quad \partial\Omega_c, \tag{36}$$

$$\|\mathbf{p}_t\|_\mu = |p_n| \Rightarrow \quad \mathbf{p}_t = -|p_n|\mathbb{M}^2\dot{\mathbf{g}}_t/\|\dot{\mathbf{g}}_t\|_\mu^* \quad \text{on} \quad \partial\Omega_c. \tag{37}$$

As stated in [64] for quasi-static frictional contact problems, the tangential slip velocity $\dot{\mathbf{g}}_t$ defined in the above expressions can be expressed at time τ_k as follows: $\dot{\mathbf{g}}_t \approx \Delta\mathbf{g}_t/\Delta\tau$, where $\Delta\mathbf{g}_t = \mathbf{g}_t(\tau_k) - \mathbf{g}_t(\tau_{k-1})$, $\Delta\tau = \tau_k - \tau_{k-1}$, and $\mathbf{g}_t = (\mathbf{u}^2 - \mathbf{u}^1) - u_n\mathbf{n}_c$, being zero the initial tangential slip. In Eq. (37), the value for the tangential contact traction was presented in reference [64] assuming an associated sliding rule, the norm $\| \bullet \|_\mu^*$ is dual of $\| \bullet \|_\mu$ $\left(i.e. \quad \|\dot{\mathbf{g}}_t\|_\mu^* = \sqrt{(\mu_1\dot{g}_{e_1})^2 + (\mu_2\dot{g}_{e_2})^2} \right)$, and $\mathbb{M}$ is a diagonal matrix: $\mathbb{M} = diag(\mu_1, \mu_2)$.

However, the ACNT fibers can be oriented with any angle ($0 \leq \phi \leq \pi/2$) relative to direction $\mathbf{e}_1$, as defined in Fig. 6 (b). Therefore, the principal friction coefficients in the directions $\{e_1, e_2\}$ has to be redefined as:

$$\mu_1 = \mu_L + (\mu_N - \mu_L)\,\hat{\phi}, \tag{38}$$

$$\mu_2 = \mu_T + (\mu_N - \mu_T)\,\hat{\phi}, \tag{39}$$

where μ_L, μ_T and μ_N are the friction coefficients in the longitudinal, transverse and normal directions, respectively, and $\hat{\phi} = 2\phi/\pi$ is the nondimensional fiber orientation angle ($0 \leq \hat{\phi} \leq 1$). The friction coefficients $\{\mu_L, \mu_T, \mu_N\}$ can be obtained from experimentation, in consonance with [30, 31].

10

According to expressions (38) and (39), the anisotropic friction surface in Eq. (35) becomes also a function of the fiber orientation angle ($\hat{\phi}$): $f(\mathbf{p}_t, p_n, \hat{\phi}) = \|\mathbf{p}_t\|_{\mu(\hat{\phi})} - |p_n| = 0$. Consequently, the frictional response of the CNTRC depends on the sliding direction (ψ) and the CNT orientation ($\hat{\phi}$). Hence, an orthotropic friction law, whose principal friction coefficients are $\mu_1 = \mu_L$ and $\mu_2 = \mu_T$, is obtained when the fibers are parallel to the sliding plane ($\hat{\phi} = 0$). An isotropic friction law (i.e. $\mu_1 = \mu_2 = \mu_N$) is obtained when the fibers are normal to the sliding plane ($\hat{\phi} = 1$).

Finally, proceeding in the same way as in the normal contact law, the frictional contact constraints Eqs. (36–37) can be also rewritten in a more compact form as:

$$\mathbf{p}_t - \mathbb{P}_{\mathbb{E}_\rho}(\mathbf{p}_t^*) = 0, \tag{40}$$

where $\mathbf{p}_t^* = \mathbf{p}_t - r_t \mathbb{M}^2 \dot{\mathbf{g}}_t$ ($r_t \in \mathbb{R}^+$) is the augmented tangential traction and $\mathbb{P}_{\mathbb{E}_\rho}(\bullet) : \mathbb{R}^2 \longrightarrow \mathbb{R}^2$ is the tangential projection function defined in [64] as:

$$\mathbb{P}_{\mathbb{E}_\rho}(\mathbf{p}_t^*) = \begin{cases} \mathbf{p}_t^* & \text{if} \quad \|\mathbf{p}_t^*\|_\mu < \rho, \\ \rho\, \mathbf{p}_t^*/\|\mathbf{p}_t^*\|_\mu & \text{if} \quad \|\mathbf{p}_t^*\|_\mu \geq \rho, \end{cases} \tag{41}$$

with ρ being the module of the projected augmented normal contact traction: $\rho = |\mathbb{P}_{\mathbb{R}_-}(p_n^*)|$.

5. Numerical considerations

Each solid Ω^l ($l = 1, 2$) have been discretized using the bounary element method [25, 26] which makes it possible to compute the elastic influence coefficients of the surface points involved in the contact [64, 65]. After a collocation procedure on each boundary $\partial\Omega^l$, the integral equations can be written as $\mathbf{Hd} = \mathbf{Gp}$, where $\mathbf{d}$ and $\mathbf{p}$ contains the values of all nodal displacements and tractions, respectively. Finally, that expression can be rearranged according to the boundary conditions as:

$$\mathbf{Ax} = \mathbf{F}, \tag{42}$$

passing all the unknowns to vector $\mathbf{x}$ on the left-hand side.

The interface discretization on $\partial\Omega_c$ is performed such that node to node contact is considered. Consequently, each node on $\partial\Omega_c^1$ forms a contact pair I with one almost coincident node on $\partial\Omega_c^2$. So, equation (42) can be written for solid Ω^l ($l = 1, 2$) as: $\mathbf{A}_x^l \mathbf{x}^l + \mathbf{A}_p^l \mathbf{p}_c^l = \mathbf{F}^l$, where $(\mathbf{x}^l)^T = [(\mathbf{x}_e^l)^T\ (\mathbf{d}_c^l)^T]$ is the nodal unknowns vector that collects the contact nodal displacements ($\mathbf{d}_c^l$) and the external unknowns ($\mathbf{x}_e^l$). $\mathbf{A}_x^l$ is constructed with the columns of matrices $\mathbf{H}^l$ and $\mathbf{G}^l$, and $\mathbf{A}_p^l$ with the columns of $\mathbf{G}^l$ belonging to the contact nodal unknowns. Therefore, the discrete equilibrium equations can be formulated as:

$$\mathbf{A}_x^1 \mathbf{x}^1 + \mathbf{A}_p^1 \tilde{\mathbf{C}}^1 \lambda = \mathbf{F}^1, \tag{43}$$

$$\mathbf{A}_x^2 \mathbf{x}^2 - \mathbf{A}_p^2 \tilde{\mathbf{C}}^2 \lambda = \mathbf{F}^2. \tag{44}$$

In Eqs. (43) and (44), the vector λ contains the normal and tangential contact tractions of every contact pair I, which are related to the boundary element nodal tractions vector through the matrix $\tilde{\mathbf{C}}^l$ (i.e. $\mathbf{p}_c^1 = \tilde{\mathbf{C}}^1 \lambda$ and $\mathbf{p}_c^2 = -\tilde{\mathbf{C}}^2 \lambda$) as described in reference [65].

The discrete gap for every contact pair I is approximated as:

$$\mathbf{g} = \mathbf{C}_{g_n} \mathbf{g}_o + (\mathbf{C}^2)^T \mathbf{x}^2 - (\mathbf{C}^1)^T \mathbf{x}^1, \tag{45}$$

where $\mathbf{g}$ contains the normal and tangential gap of every contact pair I and $\mathbf{g}_o$ contains the initial gap. $\mathbf{C}_{g_n}$ is an assembling matrix defined in [65].

Finally, the contact restrictions (34) and (40) are applied to every contact pair I:

$$(\lambda_n)_I - \mathbb{P}_{\mathbb{R}_-}((\lambda_n)_I + r_n(\mathbf{g}_n)_I) = 0, \tag{46}$$

$$(\lambda_t)_I - \mathbb{P}_{\mathbb{E}_\rho}((\lambda_t)_I - r_t \mathbb{M}^2(\mathbf{g}_t)_I) = \mathbf{0}, \tag{47}$$

where λ_n and λ_t contain the normal and tangential contact tractions of every contact pair I, respectively.

The quasi-static contact problem defined by equations (43-47) can be solved using different solution schemes according to [66] and [67]. In this work, the nonlinear system (43-47) is solved using an iterative method, namely Uzawa's method as presented in [64].

6. Results and discussion

The previously overviewed contact formulation offers a suitable framework to predict the indentation response of CNTRCs. In order to understand the influence of the main micromechanical properties of CNTs on the tribological behavior of polymer-CNT composites, as well as to extract valuable conclusions for assisting their design, detailed parametric analyses are presented in the following sections. Specifically, the numerical results focus on the analysis of the influence of the filler content, waviness, orientation distribution and agglomeration on the tribological response of polymer-CNT composites.

An adequate selection of the elastic moduli of CNTs is essential for the accuracy of the numerical simulations. The stiffening efficiency of CNTs is attributed to the load transfer mechanism from matrix to fillers through weakly non-bonded van der Waals (vdW) forces. In order to account for this atomic interaction, numerous recent publications have been conducted by the Extended Rule of Mixtures (EROM) [68, 69]. The EROM is based upon a modification of the classical Voigt and Reuss bounds by the so-termed efficiency parameters [70]. A more convenient alternative that allows the use of the previously outlined micromechanics approaches is based on the concept of equivalent fiber [71]. In this way, a portion of matrix material and an embedded CNT is replaced by an equivalent solid fiber which is apt to be used in a conventional mean-field homogenization approach. In this work, the elastic moduli of the equivalent fiber for epoxy doped with (10,10) SWCNTs are taken from the atomistic-based FEM simulations conducted by Shokrieh and Rafiee [71]. The Young's modulus and Poisson's ratio of the matrix are $E_m = 10$ GPa, $\nu_m = 0.3$, and the elastic properties of the equivalent fiber are collected in Table 1. It should be noted that the values in this table corresponds to a CNT volume fraction of 7.5%. Therefore, the inclusion volume fraction must be defined in terms of equivalent fibers (see Fig. 7) as follows:

$$f_r = v_f \frac{(D^c + t^c)^2}{4 t^c D^c} \tag{48}$$

where v_f stands for the volume fraction of CNTs, f_r the volume fraction of equivalent fibers, D^c the diameter of the CNT, and t^c the thickness of the interphase. Assuming $G_{23} = G_{12}$, the Hill's moduli in Eq. (3) can be extracted from Eqs. (4) to (8).
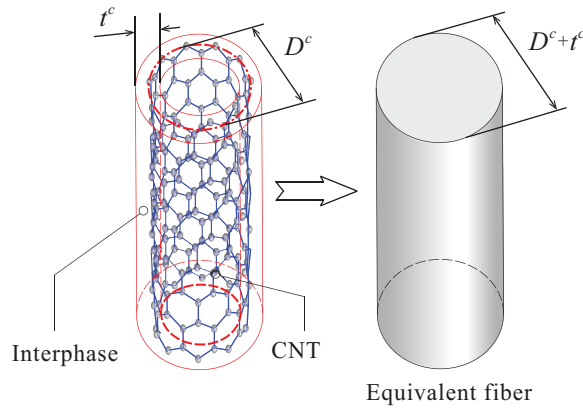

Figure 7: Schematic representation of CNT equivalent filler

Table 1: Material properties of the equivalent fiber for epoxy doped with a (10,10) SWCNT computed by atomistic-based FEM simulation [71].

Longitudinal Young's modulus (E_{11})	649.37 GPa
Transverse Young's modulus (E_{22})	11.27 GPa
Longitudinal shear modulus (G_{12})	5.13 GPa
Poisson's ratio (ν_{12})	0.284
CNT tube thickness (t^c)	0.34 nm
CNT diameter (D^c)	2.034 nm

In order to thoroughly investigate the influence of the different micromechanical variables on the tribological behavior of CNT/polymer composites, the numerical tests have been divided into five subsections: Subsection 6.1 assesses the influence of the CNT volume fraction and orientation. Subsection 6.2 investigates the tangential load response of ACNT reinforced composites. Subsection 6.3 studies the effects of filler agglomeration. Subsection 6.4 studies the effects of filler curviness and, finally, Subsection 6.4 investigates the tribological behavior of composites with simultaneous effects of filler waviness and agglomeration.

6.1. Influence of CNT volume fraction and orientation

A steel sphere of radius $R = 100 \times 10^{-3}$ m is indented on a CNTRC Half-Space (HS) domain (see Fig. 8 (a)). For that purpose, the half-space region is modeled by a square boundary area whose dimensions are $2L_1 \times 2L_1$, being $L_1 = 50 \times 10^{-3}$ m. It is discretized by linear quadrilateral boundary elements, using 16×16 elements on the $L_o \times L_o$ potential contact zone ($L_o = 5 \times 10^{-3}$ m), as shown in Fig. 8 (b). The influence of the filler volume fraction on the indentation response of randomly distributed CNTs (RCNT) and aligned distribution of CNTs (ACNT) is studied in this section, where different ACNTs orientations ϕ are also considered (see Fig. 9). In this example, the spherical indenter is subjected to a normal displacement $g_{o,x_3} = -8 \times 10^{-5}$ m and the indentation force P is computed by integration of the normal contact pressures.

(a)

(b)
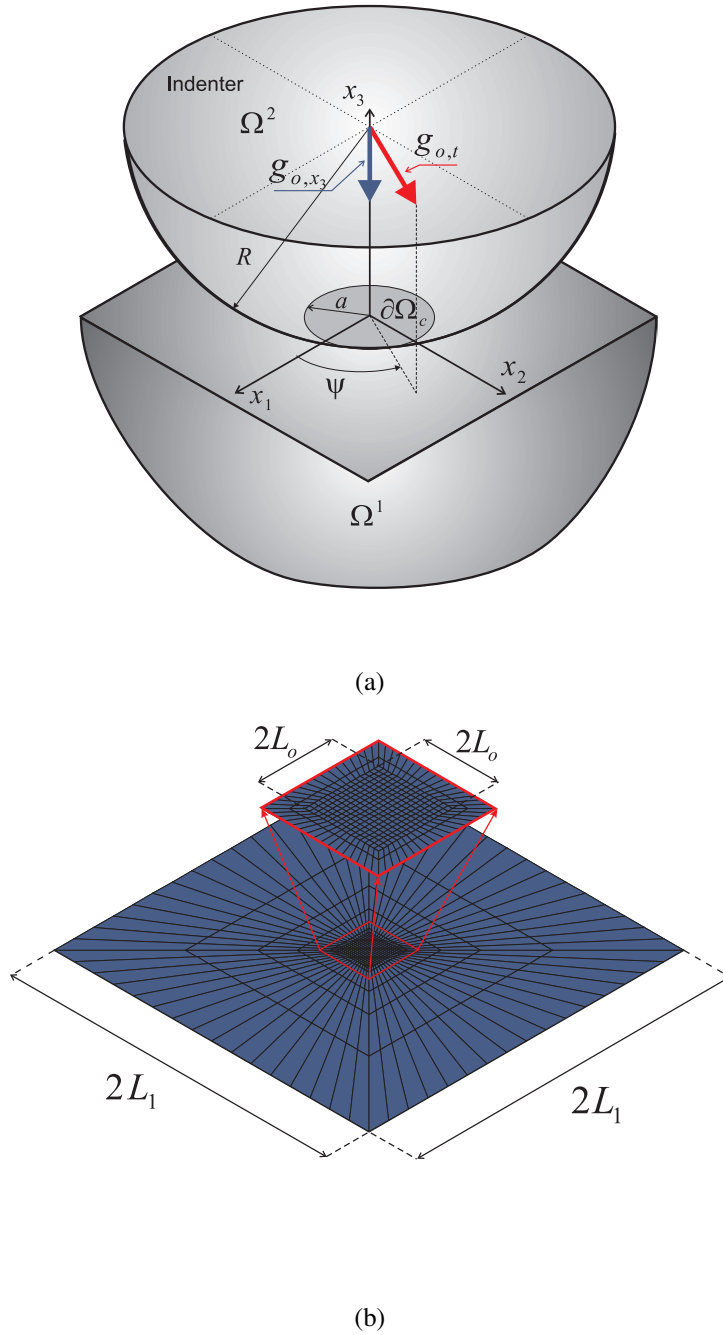
Figure 8: (a) Spherical indenter over a CNTRC half-space (HS). (b) Boundary element mesh details for the HS configuration.

13
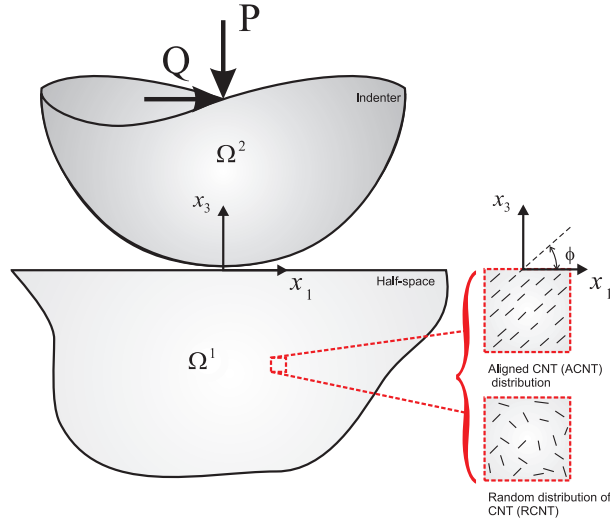
Figure 9: Two kind of CNTs distributions are considered on Ω^1: random distribution of CNTs (RCNT) or aligned distribution of CNTs (ACNT).

Fig. 10 shows the variation of the normal contact compliance with the CNT volume fraction. Different CNT contents v_f have been considered, namely 0%, 1%, 2%, 3%, 4% and 5%, as well as ACNT orientations ϕ ranging from 0 to 90°. It can be observed in both cases (RCNT and ACNT) that the normal contact compliance increases with the fiber volume fraction. In addition, it is noted that for an orientation angles ϕ greater than 45°, the ACNTs lead to greater increments.

Indentation forces as a function of the ACNT orientation ϕ and different volume fractions $v_f = \{1\%, 3\%, 5\%\}$ are presented in Fig. 11. It is noted in this figure that the normal contact compliance increases with the CNT volume fraction. Nevertheless, for fiber orientations below 45°, the normal contact compliance experiences very limited changes. It is also interesting to note that, in this range of orientations, higher fiber orientations do not lead to significant increments in the normal contact compliance. Conversely, fiber orientations within the interval [45°, 90°] do lead to increasing normal contact forces, reaching maximum values at ϕ=90° (i.e. vertical ACNTs). Larger increments are also found in this range of orientations for higher filler volume fractions. In this figure, the RCNT compliances are also presented for the same volume fractions: $v_f = \{1\%, 3\%, 5\%\}$. It can be observed that for orientation values greater than 60°, the ACNT presents a higher response than RCNT for the volume fractions considered.
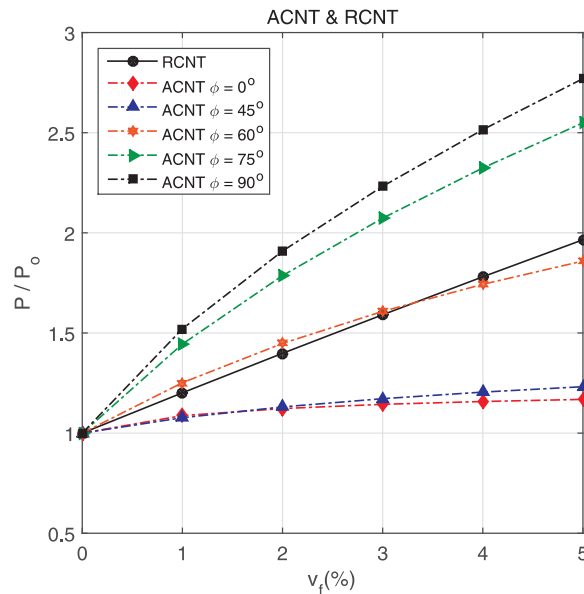

Figure 10: Indentation forces as a function of the volume fraction of CNT and CNT distributions, i.e., random distribution of CNT (RCNT) and aligned distribution of CNT (ACNT).
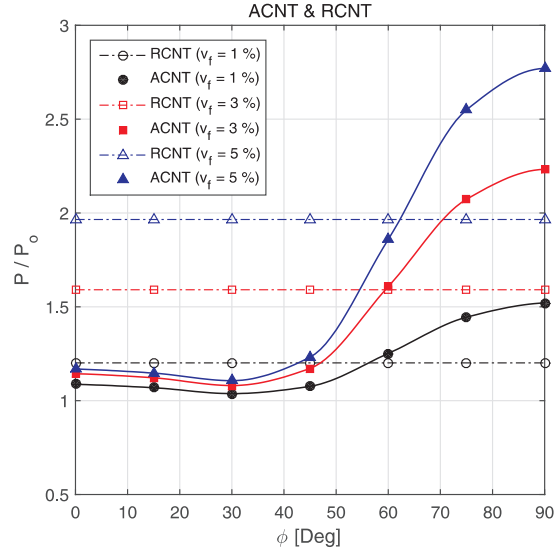
Figure 11: Indentation forces as a function of the ACNT orientation ϕ and different volume fractions: $v_f = \{1\%, 3\%, 5\%\}$.

Same behavior is observed in Fig. 12 for the normal contact pressure distributions. They are presented as a function of the CNTs volume fractions $v_f = \{0\%, 1\%, 3\%, 5\%\}$ relative to the pristine polymer hertzian contact pressure distribution. Fig. 12 (a) shows the RCNT distribution and Fig. 12 (b-d) shows the contact pressures for ACNT for: $\phi = 0°$, $\phi = 45°$ and $\phi = 90°$, respectively. The CNT distribution and CNT volume fraction have a tremendous influence on the normal contact pressure and consequently, on the contact response. The maximum contact pressure for RCNT distributions is highly affected by the volume fraction. However, the maximum contact pressure for ACNT is only affected significantly when the CNTs orientations are greater than 45°. In those orientations, the normal contact compliance for ACNT is much higher than for RCNT, for the same volume fraction. This phenomenon is interesting to develop high performance contact surfaces or smart coatings. Finally, it should be noted in Fig. 13 that the shape and dimension of the effective contact zone (a circle of radius $a = 2.8$ *mm*) does not depend on the orientation of CNTs.
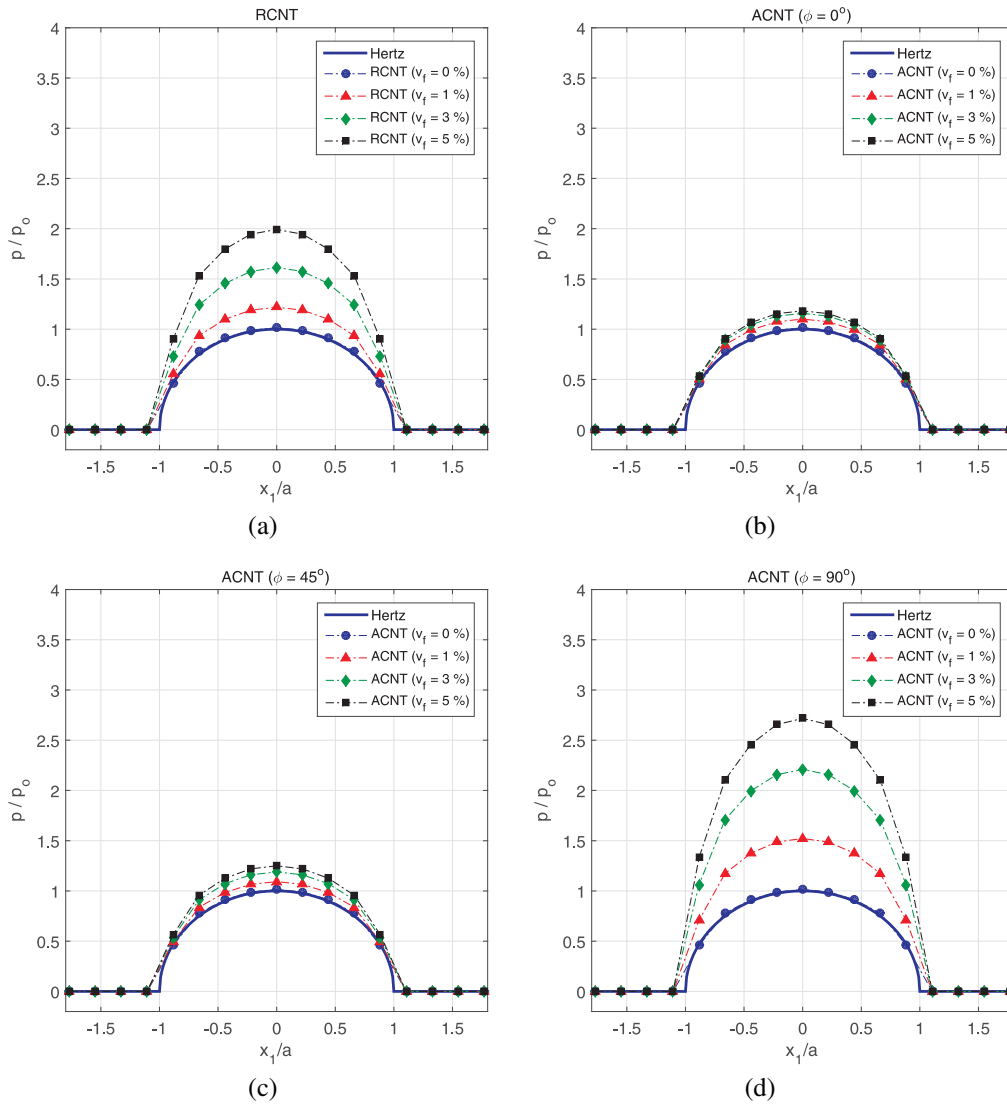
Figure 12: Normal contact pressure distribution as a function of the CNTs distribution and ACNT orientation: (a) RCNT distribution, (b) ACNT ($\phi = 0°$), (c) ACNT ($\phi = 45°$) and (d) ACNT ($\phi = 90°$).
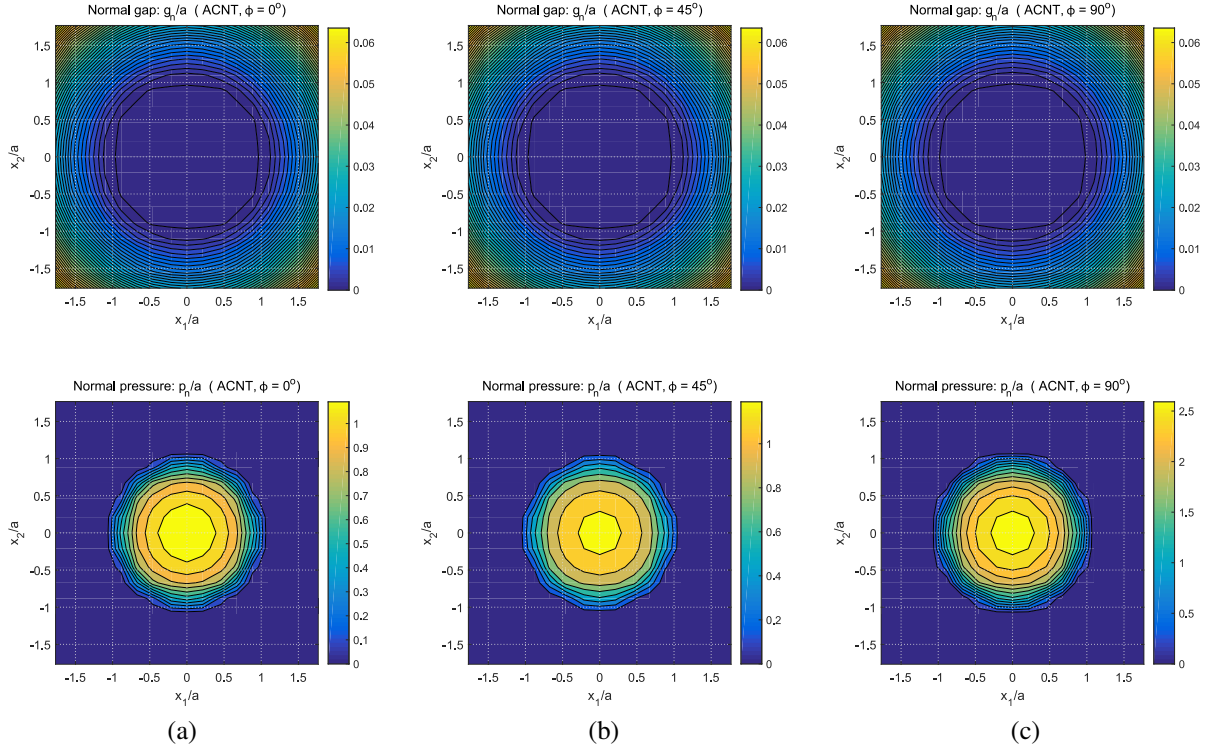
Figure 13: Contact gap and normal contact pressure distributions for ACNT distribution as a function of the CNTs orientations: (a) $\phi = 0°$, (b) $\phi = 45°$ and (c) $\phi = 90°$.

6.2. Tangential load response of ACNT reinforced composites

The influence of the fiber orientation (ϕ) on the tangential load response under partial slip and gross slip conditions is considered in this section. The tangential contact compliance (Q) is analyzed for an ACNT reinforced HS configuration (see Fig. 9). In this example, the spherical indenter is subjected to a normal displacement $g_{o,x_3} = -8 \times 10^{-5}$ m and a tangential translational displacement of module $g_{o,t}$ which forms an angle ψ with axis x_1 (see Fig. 8 (a)).

The friction coefficients for this ACNT reinforced composite are: $\mu_L = 0.77$, $\mu_T = 0.82$, $\mu_N = 0.67$. They have been considered from reference [31] for a 1% ACNT/epoxy composite. The isotropic friction coefficient for the epoxy is $\mu = 0.9$. Wan *et al.* [31] showed that the presence of ACNTs can reduce significantly the friction coefficients of epoxy composites under gross slip conditions. In this example, the influence of the fiber orientation (ϕ) for $v_f = 1\%$ ACNT-RC is studied in Fig. 14, where Q/P is presented for two tangential loads: $g_{o,t} = 10 \times 10^{-5}$ m (i.e. gross slip conditions) and $g_{o,t} = 4 \times 10^{-5}$ m (i.e. partial slip conditions). Gross slip conditions makes it possible to validate the isotropic and anisotropic friction laws considered, i.e., we can see how the friction coefficients are recovered: 0.9 for the epoxy and $\mu_L = 0.77$ and $\mu_N = 0.67$ in the ACNT/epoxy for $\phi = 0°$ and $\phi = 90°$, respectively. As expected, the friction coefficient of epoxy is reduced by the presence of ACNT. On the other hand, we can see in Fig. 14 that this reduction is not so severe under partial slip conditions, i.e., $g_{o,t} = 4 \times 10^{-5}$ m, and it appears only for orientation values greater than 45°.

Fig. 15 shows the influence of the fiber orientation (ϕ) and the sliding direction (ψ) in the tangential contact force relative to the epoxy configuration, under partial slip conditions. The minimum values for the normalized tangential contact load (Q) occur for a fiber orientation $\phi = 45°$, whereas the maximum values occur for $\phi = 0°$. The tangential contact force is significantly affected by the CNTs orientation, with differences up to 10 % between tangential forces observed for $\phi = 0°$ and $\phi = 45°$. In these angles, some discrepancies are observed for the different sliding directions: $\psi = 0°$ and $\psi = 90°$}. However, the tangential force is not affected by ψ for $\phi = 90°$. This is because we recover the isotropic frictional behavior ($\mu_1 = \mu_2 = \mu_N$) when $\phi = 90°$.
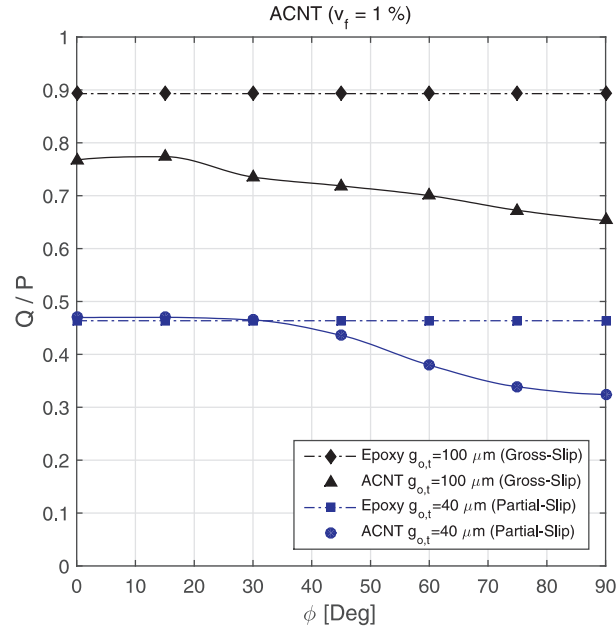
17

Figure 14: Influence of the fiber orientation on the tangential load response under partial slip and gross slip conditions.
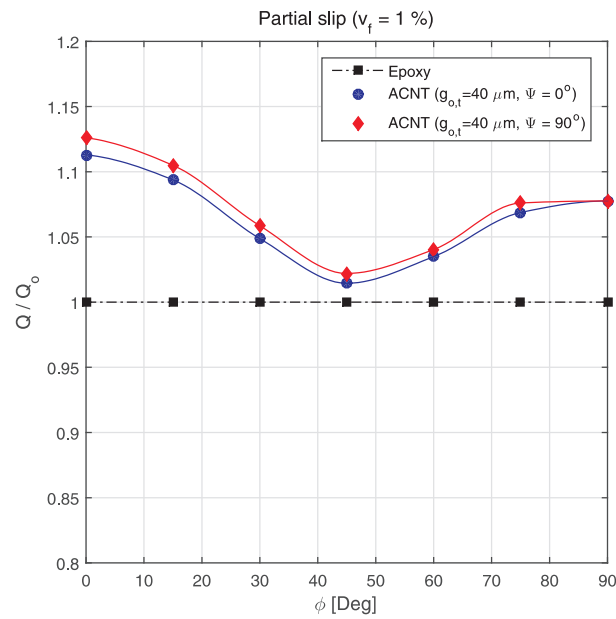

Figure 15: Influence of the fiber orientation (ϕ) and the sliding direction (ψ) in the tangential contact force relative to the epoxy configuration, under partial slip conditions.

Same differences can be observed in Fig. 16 where the influence of the fiber orientation (ϕ) in the tangential contact force relative to the epoxy configuration is presented for gross and partial slip conditions. Under gross slip conditions, the tangential contact force is even more affected by the CNTs orientation, with differences close to 30 % between tangential forces observed for $\phi = 45°$ and $\phi = 90°$. Finally, Fig. 17 shows the contact traction distributions at $x_2 = 0$ for: (a) $\phi = 0°$, (b) $\phi = 45°$ and (c) $\phi = 90°$, under partial slip conditions ($g_{o,t} = 8 \times 10^{-5}$ m). These figures show how the contact slip and stick zones are affected by the CNT orientation.
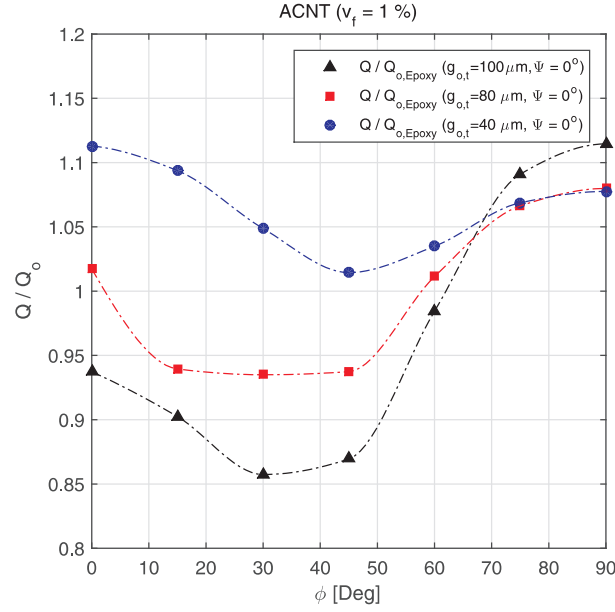
Figure 16: Influence of the fiber orientation (ϕ) in the tangential contact force relative to the epoxy configuration, under partial slip and gross slip conditions.
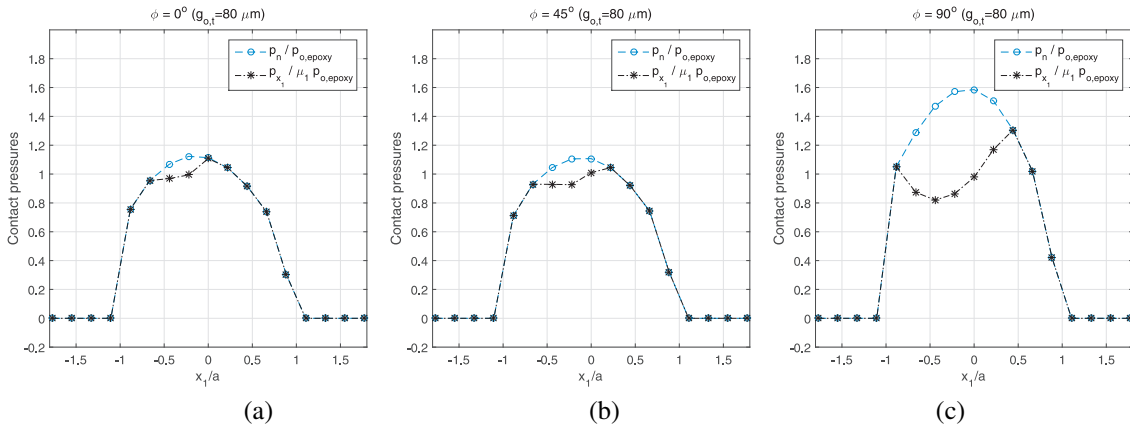

Figure 17: Influence of fiber orientation in the contact tractions at $x_2 = 0$ for: (a) $\phi = 0°$, (b) $\phi = 45°$ and (c) $\phi = 90°$.

6.3. Effect of filler agglomeration on the indentation response

As previously mentioned in Section 3.3, an important phenomenon to be taken into account in the simulation of CNT-based composites is the appearance of non-uniform spatial distributions of nanoinclusions due to their tendency to form agglomerates. Fig. 18 presents the indentation response of aligned and randomly distributed CNT-polymer nanocomposites as a function of the ACNT orientation ϕ and the agglomeration parameters: $\xi = 0.2$ and $\zeta = \{0.2, 0.4, 0.6, 0.8\}$, being $v_f = 5\%$. It can be observed that when the ζ parameter increases, that is to say, the volume ratio of CNTs within the bundles with respect to the total volume of fillers, the normal contact compliance decreases. In general, this phenomenon is more significant in RCNT than in ACNT. However, when the fiber orientations are greater than 60°, the effect of filler agglomeration is more severe in ACNT than in RCNT. This can be clearly observed in Fig. 19. The normal contact compliance of ACNT is almost not affected by the agglomerations effects for fiber orientations within the interval $[0°, 45°]$, whilst it is clearly affected when the orientation is greater than 45°. Specially when it is greater than 60°. The indentation force presents differences up to 30 % between the CNTRC with uniform filler dispersion ($\zeta = 0.2$) and the CNTRC with a high number of agglomerates $\zeta = 0.8$.
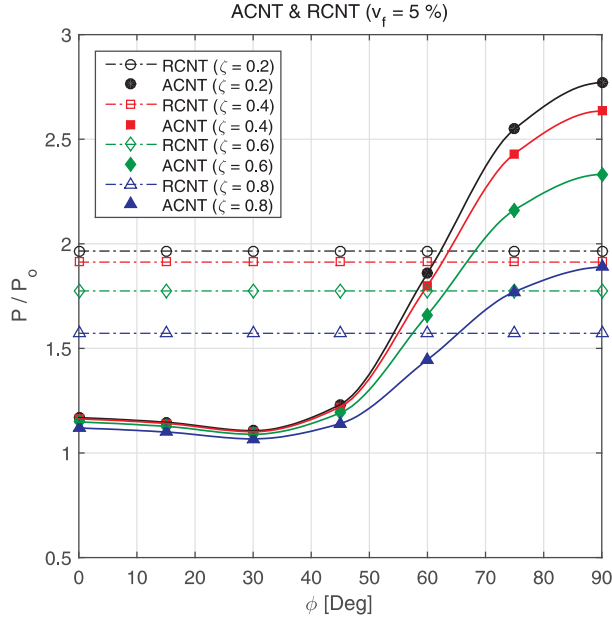
Figure 18: Indentation forces for RCNT and ACNT as a function of the ACNT orientation ϕ and the agglomeration parameter: $\zeta = \{0.2, 0.4, 0.6, 0.8\}$.
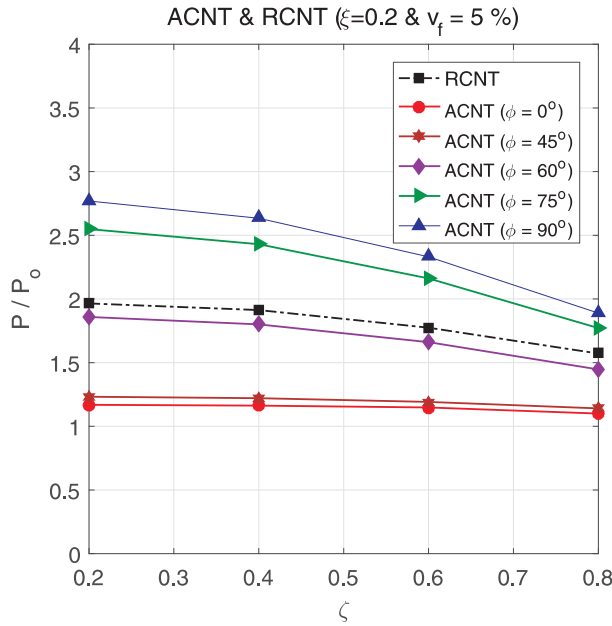

Figure 19: Effect of filler agglomeration on the indentation response of randomly distributed CNT-polymer nanocomposites (RCNT) and aligned distributed CNT-polymer nanocomposites (ACNT).

6.4. Effect of waviness on the indentation response

Another important aspect to consider is how the indentation force is affected by the CNTs waviness. So, in this section, the indentation response of wavy CNT-reinforced polymer composites is analyzed. Two CNT configurations have been considered, namely, RCNT and vertical ACNT ($\phi = 90°$), and different waviness parameters $\theta = \{90°, 80°, 70°, 60°\}$ have been studied for $v_f = 5\%$. Results in Fig. 20 show that the indentation force is not significantly affected by the CNTs waviness, although a slight reduction can be observed when the waviness increases, i.e., θ reduces to $60°$. Fig. 21 shows the same effect of waviness on the contact pressure distribution of randomly distributed CNT-polymer nanocomposites (Fig. 21 (a)) and aligned distributed CNT-polymer nanocomposites Fig. 21 (b). A reduction in the maximum contact pressure of 10 percent is observed in both CNT distributions.
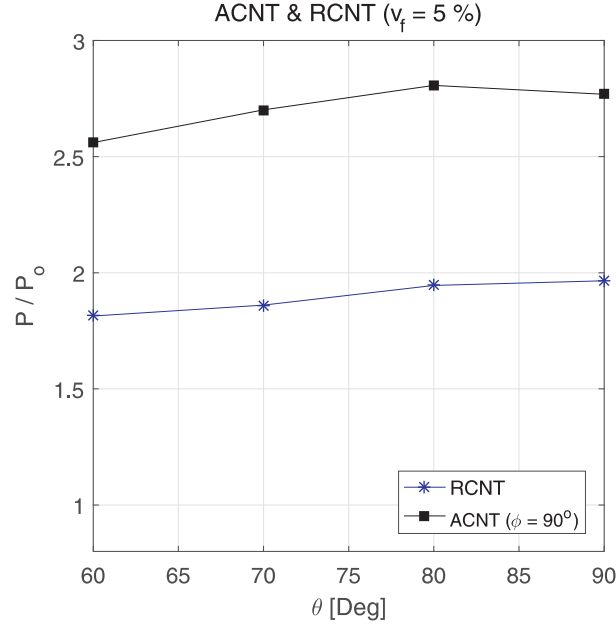
Figure 20: Effect of waviness on the indentation response of RCNT and ACNT.
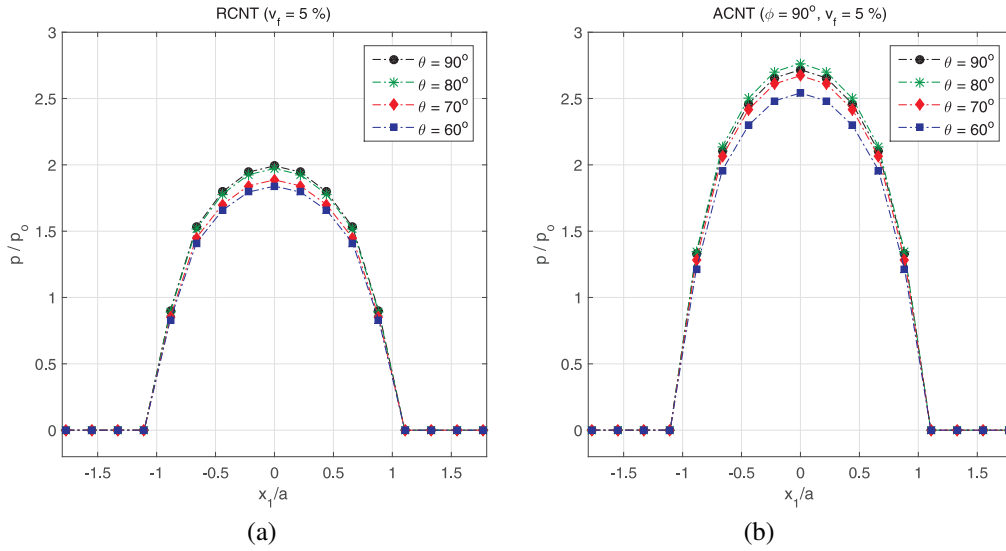

(a)

(b)

Figure 21: Effect of waviness on the contact pressure distribution of: (a) randomly distributed CNT-polymer nanocomposites and (b) vertically aligned distributed CNT-polymer nanocomposites.

6.5. Coupled effect of CNTs waviness and agglomeration

Finally, the coupled effect of CNTs waviness and agglomeration on the indentation response of CNTRC is considered. Fig. 22 shows the effect of agglomeration in the indentation response of wavy and straight randomly distributed CNT-polymer nanocomposites and vertically aligned distributed CNT-polymer nanocomposites. It is noted that the decreases in the indentation force induced by waviness and agglomeration effects add up when both phenomena act simultaneously. Therefore, it can be concluded that both agglomeration and waviness act as defects in the microstructure, and the omission of their coupled effect may lead to overestimations of the tribological behavior of CNTRCs. It is also observed in Fig. 22 that the filler agglomeration presents a higher influence on the indentation response than the waviness. Moreover, that influence is more severe in vertically aligned distributed CNT-polymer nanocomposites than in randomly distributed CNT-polymer nanocomposites. Fig. 23 (a) shows a reduction in the maximum contact pressure of 18 percent, whereas Fig. 23 (b) shows a reduction in the maximum contact pressure of 30 percent. Therefore, it is clear that the modeling agglomeration effects in CNT-polymer nanocomposites is a key aspect to accurately predict the indentation behavior of CNT-polymer nanocomposites.
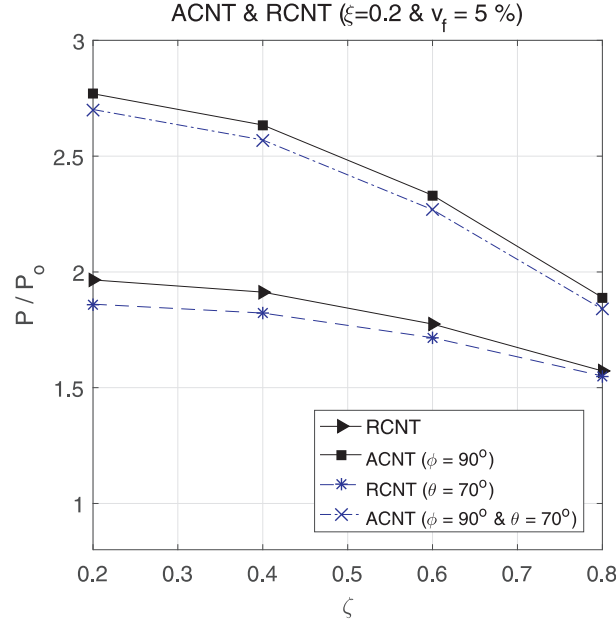
Figure 22: Coupled effect of CNTs waviness and agglomeration on the indentation response.
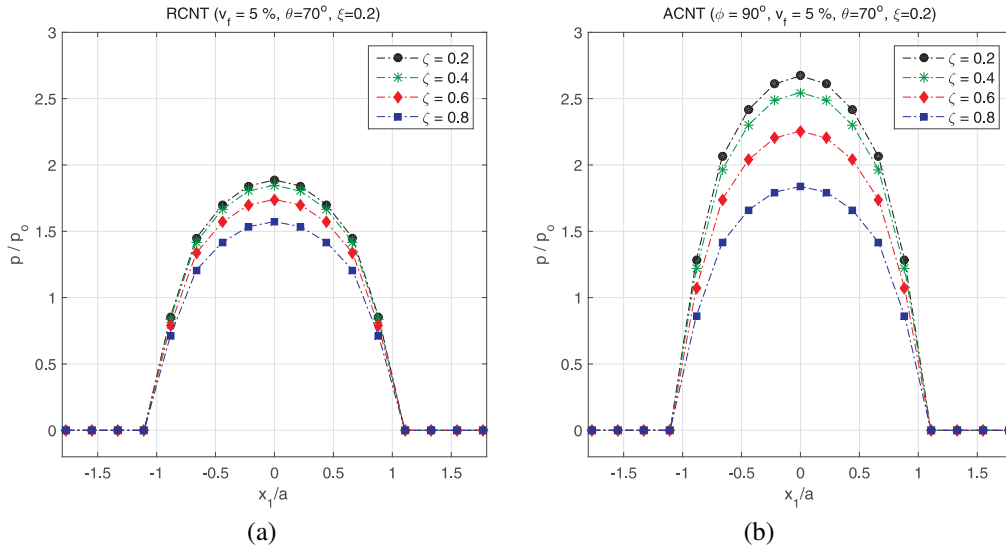

(a)

(b)

Figure 23: Coupled effect of CNTs waviness and agglomeration on the contact pressure distribution of: (a) randomly distributed CNT-polymer nanocomposites and (b) aligned distributed CNT-polymer nanocomposites (ACNT).

7. Concluding remarks

The influence of micromechanical properties on the indentation response of CNTRCs has been studied. The effective constitutive properties of the composites have been predicted by an Eshelby-Mori-Tanaka micromechanical model. This model allows us to consider aligned CNTs distributions or to simulate more realistic features typically reported for CNT-reinforced polymers, i.e. waviness and agglomeration effects. A 3D boundary element formulation, which has been proved to be very robust and accurate for this kind of contact simulations, provides the elastic influence coefficients for the CNT reinforced half-space. Moreover, in order to study uniaxially-aligned CNT reinforced composites under frictional indentation conditions, an anisotropic friction constitutive law has been considered. This contact constitutive law allowed us to assess the influence of the fiber orientation (ϕ) on the friction coefficients. The proposed methodology has been applied to study the indentation response of CNTRC half-space and the influence of the micromechanical properties on the contact compliances. Results reveal that the micromechanical aspects of CNTs have to be taken into account on contact simulation. In other case, we could over- or underestimate contact magnitudes. For instance, fibers orientation has a fundamental effect on normal and

22

tangential contact compliances or on contact traction magnitude and distribution. In this way, we may maximize the effectiveness of the reinforcement and therefore the properties of the CNTRC, by controlling the CNT fiber alignment, dispersion or volume fraction. Finally, it should be noted that the proposed methodology can be useful in developing experimental indentation tests to extract the mechanical and tribological properties of ACNT reinforced composites and to design new CNT reinforced mechanical systems with better resistance under frictional contact condition.

The key findings of this work can be summarized as follows:

- In the case of uniaxially-aligned filler configurations, the numerical results have demonstrated that filler orientations in the range $\phi \in [45°, 90°]$ yield the highest normal contact forces, with maximum values at $\phi = 90°$, that is to say, fillers aligned with the indenter. In addition, while higher filler contents lead to stiffer responses of the composites for filler orientations in the range $\phi \in [45°, 90°]$, only a limited stiffening efficiency has been found for filler orientations below $\phi = 45°$.

- The numerical results have demonstrated that the indentation force of CNTRCs is higher for uni-axially filler configurations when $\phi \in [60°, 90°]$ compared to random distributions, whilst random filler configurations yield higher indentation forces than those obtained for ACNTs with $\phi \in [0°, 60°]$.

- The analyses on the tangential response of ACNT-reinforced composites have showed that the filler orientation exhibits a substantial influence on their tribological response. It has been reported that minimum values of tangential loads are found at filler orientations of $\phi = 45°$, whereas maximum values occur at $\phi = 0°$. Additionally, it has been shown that the filler orientation has a higher influence on the tangential forces when gross slip conditions are considered, finding differences up to 30 % between the forces observed for $\phi = 45°$ and $\phi = 90°$.

- The numerical analyses evidence the detrimental effects of filler waviness and agglomerations which act as microstructural defects. Additionally, the simultaneous consideration of waviness and agglomeration on the indentation response of CNTRCs have demonstrated that their weakening effects add up.

Finally, it should be remarked that the present numerical framework is general and does not limit to only studying the indentation response of the half-space CNT nanocomposite configurations presented in this paper. The BEM approach implemented herein can be easily extended to analyze for instance smart nanocomposite coatings involving thin film geometries [72], e.g., a bearing covered by a CNT nanocomposite layer, or any other high performance contact surfaces configurations.

References

[1] J. N. Coleman, U. Khan, W. J. Blau, Y. K. Gun'ko, Small but strong: A review of the mechanical properties of carbon nanotube–polymer composites, Carbon 44 (2006) 1624–1652.

[2] R. F. Gibson, A review of recent research on mechanics of multifunctional composite materials and structures, Composite Structures 92 (2010) 2793–2810.

[3] F. Ubertini, S. Laflamme, H. Ceylan, A. L. Materazzi, G. Cerni, H. Saleem, A. D'Alessandro, A. Corradini, Novel nanocomposite technologies for dynamic monitoring of structures: a comparison between cement-based embeddable and soft elastomeric surface sensors, Smart Materials and Structures 23 (2014) 045023.

[4] E. García-Macías, A. Downey, A. D'Alessandro, R. Castro-Triguero, S. Laflamme, F. Ubertini, Enhanced lumped circuit model for smart nanocomposite cement-based sensors under dynamic compressive loading conditions, Sensors and Actuators A: Physical 260 (2017) 45–57.

[5] B. J. Briscoe, S. K. Sinha, Tribological applications of polymers and their composites: Past, present and future prospects, in: Tribology of Polymeric Nanocomposites - Friction and Wear of Bulk Materials and Coatings, Elsevier, 2008, pp. 1–14.

[6] K. Friedrich, Friction and wear of polymer composites, volume 1, Elsevier, 2012.

[7] M. R. Ayatollahi, S. Doagou-Rad, S. Shadlou, Nano-/microscale investigation of tribological and mechanical properties of epoxy/MWNT nanocomposites, Macromolecular Materials and Engineering 297 (2012) 689–701.

[8] M. K. Yeh, T. H. Hsieh, N. H. Tai, Fabrication and mechanical properties of multi-walled carbon nanotubes/epoxy nanocomposites, Materials Science and Engineering: A 483-484 (2008) 289–292.

[9] H. Cai, F. Yan, Q. Xue, Investigation of tribological properties of polyimide/carbon nanotube nanocomposites, Materials Science and Engineering: A 364 (2004) 94–100.

[10] Y. Gao, Z. Wang, Q. Ma, G. Tang, J. Liang, A study on the wear resistance of nano-material/E 51, Cailiao Kexue Yu Jishu(J. Mater. Sci. Technol.)(China) 20 (2004) 340–343.

[11] L. Zhang, I. Zarudi, K. Xiao, Novel behaviour of friction and wear of epoxy composites reinforced by carbon nanotubes, Wear 261 (2006) 806–811.

[12] N. W. Khun, H. Zhang, J. Yang, E. Liu, Mechanical and tribological properties of epoxy matrix composites modified with microencapsulated mixture of wax lubricant and multi-walled carbon nanotubes, Friction 1 (2013) 341–349.

[13] A. K. Dutta, D. Penumadu, B. Files, Nanoindentation testing for evaluating modulus and hardness of single-walled carbon nanotube-reinforced epoxy composites, Journal of Materials Research 19 (2004) 158–164.

[14] X. Li, H. Gao, W. A. Scrivens, D. Fei, X. Xu, M. A. Sutton, A. P. Reynolds, M. L. Myrick, Nanomechanical characterization of single-walled carbon nanotube reinforced epoxy composites, Nanotechnology 15 (2004) 1416.

[15] H. J. Qi, K. B. K. Teo, K. K. S. Lau, M. C. Boyce, W. I. Milne, J. Robertson, K. K. Gleason, Determination of mechanical properties of carbon nanotubes and vertically aligned carbon nanotube forests using nanoindentation, Journal of the Mechanics and Physics of Solids 51 (2003) 2213–2237.

[16] J. F. Waters, P. R. Guduru, M. Jouzi, J. M. Xu, T. Hanlon, S. Suresh, Shell buckling of individual multiwalled carbon nanotubes using nanoindentation, Applied Physics Letters 87 (2005) 103109.

[17] C. M. McCarter, R. F. Richards, S. D. Mesarovic, C. D. Richards, D. F. Bahr, D. McClain, J. Jiao, Mechanical compliance of photolithographically defined vertically aligned carbon nanotube turf, Journal of Materials Science 41 (2006) 7872–7878.

[18] S. D. Mesarovic, C. M. McCarter, D. F. Bahr, H. Radhakrishnan, R. F. Richards, C. D. Richards, D. McClain, J. Jiao, Mechanical behavior of a carbon nanotube turf, Scripta Materialia 56 (2007) 157–160.

[19] S. Pathak, Z. G. Cambaz, S. R. Kalidindi, J. G. Swadener, Y. Gogotsi, Viscoelasticity and high buckling stress of dense carbon nanotube brushes, Carbon 47 (2009) 1969–1976.

[20] Y. C. Lu, J. Joseph, Q. Zhang, M. R. Maschmann, L. Dai, J. Baur, Large-displacement indentation testing of vertically aligned carbon nanotube arrays, Experimental Mechanics 52 (2012) 1551–1554.

[21] L. Jiang, S. M. Spearing, M. A. Monclus, N. M. Jennett, Formation and mechanical characterisation of su8 composite films reinforced with horizontally aligned and high volume fraction cnts, Composites Science and Technology 71 (2011) 1301–1308.

[22] M. T. Le, S. C. Huang, Mechanical characterization of carbon nanotube-reinforced polymer nanocomposite by nanoindentation using finite element method, Sensors and Materials 27 (2015) 617–624.

[23] H. Liu, J. W. McBride, M. P. Down, S. H. Pu, Finite element model of a bilayered gold-coated carbon nanotube composite surface, IEEE Transactions on Components, Packaging and Manufacturing Technology 5 (2015) 779–787.

[24] H. Liu, J. W. McBride, Finite-element contact modeling of rough surfaces applied to au-coated carbon nanotube composites, IEEE Transactions on Components, Packaging and Manufacturing Technology 7 (2017) 329–337.

[25] C. A. Brebbia, J. Dominguez, Boundary elements: an introductory course, WIT press, 1994.

[26] M. H. Aliabadi, The Boundary Element Method: Vol. 2. Applications in Solids and Structures., John Wiley and Sons Ltd, 2002.

[27] Y. Liu, N. Nishimura, Y. Otani, Large-scale modeling of carbon-nanotube composites by a fast multipole boundary element method, Computational Materials Science 34 (2005) 173–187.

[28] Y. J. Liu, N. Nishimura, D. Qian, N. Adachi, Y. Otani, V. Mokashi, A boundary element method for the analysis of cnt/polymer composites with a cohesive interface model based on molecular dynamics, Engineering Analysis with Boundary Elements 32 (2008) 299–308.

[29] F. C. d. Araújo, E. F. d'Azevedo, L. J. Gray, Boundary-element parallel-computing algorithm for the microstructural analysis of general composites, Computers & Structures 88 (2010) 773–784.

[30] H. Zhang, L. Qiu, H. Li, Z. Zhang, Z. Yang, H. Peng, Aligned carbon nanotube/polymer composite film with anisotropic tribological behavior, Journal of Colloid and Interface Science 395 (2013) 322–325.

[31] H. Wang, L. Chang, X. Yang, L. Yuan, L. Ye, Y. Zhu, A. T. Harris, A. I. Minett, P. Trimby, K. Friedrich, Anisotropy in tribological performances of long aligned carbon nanotubes/polymer composites, Carbon 67 (2014) 38–47.

[32] E. García, A. Hart, B. Wardle, A. Slocum, Fabrication and nanocompression testing of aligned carbon-nanotube–polymer nanocomposites, Advanced Materials 19 (2007) 2151–2156.

[33] Y. Lan, Y. Wang, Z. F. Ren, Physics and applications of aligned carbon nanotubes, Advances in Physics 60 (2011) 553–678.

[34] M. S. Al-Haik, H. Garmestani, D. S. Li, M. Y. Hussaini, S. S. Sablin, R. Tannenbaum, K. Dahmen, Mechanical properties of magnetically oriented epoxy, Journal of Polymer Science Part B: Polymer Physics 42 (2004) 1586–1600.

[35] W. Salalha, Y. Dror, R. L. Khalfin, Y. Cohen, A. L. Yarin, E. Zussman, Single-walled carbon nanotubes embedded in oriented polymeric nanofibers by electrospinning, Langmuir 20 (2004) 9852–9855.

[36] A. Joseph Berkmans, S. Ramakrishnan, G. Jain, P. Haridoss, Aligning carbon nanotubes, synthesized using the arc discharge technique, during and after synthesis, Carbon 55 (2013) 185–195.

[37] S. Nemat-Nasser, M. Hori, Micromechanics: overall properties of heterogeneous materials, volume 37, Elsevier, 2013.

[38] F. Tornabene, N. Fantuzzi, M. Bacciocchi, E. Viola, Effect of agglomeration on the natural frequencies of functionally graded carbon nanotube-reinforced laminated composite doubly-curved shells, Composites Part B: Engineering 89 (2016) 187–218.

[39] F. Tornabene, M. Bacciocchi, N. Fantuzzi, J. N. Reddy, Multiscale approach for three–phase CNT/polymer/fiber laminated nanocomposite structures, Polymer Composites (2017).

[40] T. Mori, K. Tanaka, Average stress in matrix and average elastic energy of materials with misfitting inclusions, Acta Metallurgica 21 (1973) 571–574.

[41] J. D. Eshelby, The determination of the elastic field of an ellipsoidal inclusion, and related problems, Proceedings of the Royal Society A: Mathematical, Physical and Engineering Sciences 241 (1957) 376–396.

[42] J. D. Eshelby, The elastic field outside an ellipsoidal inclusion, Proceedings of the Royal Society A: Mathematical, Physical and Engineering Sciences 252 (1959) 561–569.

[43] Y. Benveniste, G. Dvorak, T. Chen, On diagonal and elastic symmetry of the approximate effective stiffness tensor of heterogeneous media, Journal of the Mechanics and Physics of Solids 39 (1991) 927–946.

[44] T. Mura, Micromechanics of defects in solids, Springer Science & Business Media, 2013.

[45] J. Schjødt-Thomsen, R. Pyrz, The mori–tanaka stiffness tensor: diagonal symmetry, complex fibre orientations and non-dilute volume fractions, Mechanics of Materials 33 (2001) 531–544.

[46] M. S. P. Shaffer, A. H. Windle, Fabrication and characterization of carbon nanotube/poly(vinyl alcohol) composites, Advanced Materials 11 (1999) 937–941.

[47] B. Vigolo, Macroscopic fibers and ribbons of oriented carbon nanotubes, Science 290 (2000) 1331–1334.

[48] R. H. Poelma, X. Fan, Z. Y. Hu, G. V. Tendeloo, H. W. van Zeijl, G. Q. Zhang, Effects of nanostructure and coating on the mechanics of carbon nanotube arrays, Advanced Functional Materials 26 (2016) 1233–1242.

[49] D. L. Shi, X. Q. Feng, Y. Y. Huang, K. C. Hwang, H. Gao, The effect of nanotube waviness and agglomeration on the elastic property of carbon nanotube-reinforced composites, Journal of Engineering Materials and Technology 126 (2004) 250.

[50] K. Yanase, S. Moriyama, J. W. Ju, Effects of CNT waviness on the effective elastic responses of CNT-reinforced polymer composites, Acta Mechanica 224 (2013) 1351–1364.

[51] A. Allaoui, Mechanical and electrical properties of a MWNT/epoxy composite, Composites Science and Technology 62 (2002) 1993–1998.

[52] H. Li, H.-G. Xiao, J. Yuan, J. Ou, Microstructure of cement mortar with nano-particles, Composites Part B: Engineering 35 (2004) 185–189.

[53] J. M. Wernik, S. A. Meguid, Recent developments in multifunctional nanocomposites using carbon nanotubes, Applied Mechanics Reviews 63 (2010) 050801.

[54] A. Sobolkina, V. Mechtcherine, V. Khavrus, D. Maier, M. Mende, M. Ritschel, A. Leonhardt, Dispersion of carbon nanotubes and its influence on the mechanical properties of the cement matrix, Cement and Concrete Composites 34 (2012) 1104–1113.

[55] N. Fantuzzi, F. Tornabene, M. Bacciocchi, R. Dimitri, Free vibration analysis of arbitrarily shaped Functionally Graded Carbon Nanotube-reinforced plates, Composites Part B: Engineering 115 (2017) 384–408.

[56] F. Tornabene, N. Fantuzzi, M. Bacciocchi, Linear static response of nanocomposite plates and shells reinforced by agglomerated carbon nanotubes, Composites Part B: Engineering 115 (2017) 449–476.

[57] D. Banić, M. Bacciocchi, F. Tornabene, A. J. M. Ferreira, Influence of Winkler-Pasternak foundation on the vibrational behavior of plates and shells reinforced by agglomerated carbon nanotubes, Applied Sciences 7 (2017) 1228.

[58] S. C. Lin, T. Mura, Elastic fields of inclusions in anisotropic media (II), Physica Status Solidi (a) 15 (1973) 281–285.

[59] R. Michalowski, Associated and non-associated sliding rules in contact friction problems, Archiv. Mech. 30 (1978) 259–276.

[60] A. Zmitrowicz, Mathematical descriptions of anisotropic friction, International Journal of Solids and Structures 25 (1989) 837–862.

[61] Z. Mróz, S. Stupkiewicz, An anisotropic friction and wear model, International Journal of Solids and Structures 31 (1994) 1113–1131.

[62] Z. Q. Feng, M. Hjiaj, G. De Saxcé, Z. Mróz, Effect of frictional anisotropy on the quasistatic motion of a deformable solid sliding on a planar surface, Computational Mechanics 37 (2006) 349–361.

[63] Z. Q. Feng, M. Hjiaj, G. De Saxcè, Z. Mróz, Influence of frictional anisotropy on contacting surfaces during loading/unloading cycles, International Journal of Non-Linear Mechanics 41 (2006) 936–948.

[64] L. Rodríguez-Tembleque, R. Abascal, Fast FE-BEM algorithms for orthotropic frictional contact, International Journal for Numerical Methods in Engineering 94 (2013) 687–707.

[65] L. Rodríguez-Tembleque, R. Abascal, A FEM-BEM fast methodology for 3D frictional contact problems, Computers & Structures 88 (2010) 924–937.

[66] N. Kikuchi, J. T. Oden, Contact problems in elasticity: a study of variational inequalities and finite element methods, SIAM, 1988.

[67] P. Alart, A. Curnier, A mixed formulation for frictional contact problems prone to newton like solution methods, Computer Methods in Applied Mechanics and Engineering 92 (1991) 353–375.

[68] E. García-Macías, R. Castro-Triguero, E. I. S. Flores, M. I. Friswell, R. Gallego, Static and free vibration analysis of functionally graded carbon nanotube reinforced skew plates, Composite Structures 140 (2016) 473–490.

[69] Y. Kiani, Thermal post-buckling of FG-CNT reinforced composite plates, Composite Structures 159 (2017) 299–306.

[70] H. Shen, Nonlinear bending of functionally graded carbon nanotube-reinforced composite plates in thermal environments, Composite Structures 91 (2009) 9–19.

[71] M. M. Shokrieh, R. Rafiee, On the tensile behavior of an embedded carbon nanotube in polymer matrix with non-bonded interphase region, Composite Structures 92 (2010) 647–652.

[72] L. Rodríguez-Tembleque, A. Sáez, M. H. Aliabadi, Indentation response of piezoelectric films under frictional contact, International Journal of Engineering Science 107 (2016) 36–53.